Influence of the geometry on the two- and three-dimensional dynamics of the flow in a 180° sharp bend

Zhang, L. and Potherat, A.

Influence of the geometry on the two- and three-dimensional dynamics of the flow in a 180° sharp bend

Lintao Zhang and Alban Pothérat

Citation: Physics of Fluids (1994-present) **25**, 053605 (2013); doi: 10.1063/1.4807070
View online: http://dx.doi.org/10.1063/1.4807070
View Table of Contents: http://scitation.aip.org/content/aip/journal/pof2/25/5?ver=pdfcov
Published by the AIP Publishing

PHYSICS OF FLUIDS **25**, 053605 (2013)

Influence of the geometry on the two- and three-dimensional dynamics of the flow in a 180° sharp bend

Lintao Zhang[1,2,a)] and Alban Pothérat[1,b)]
[1]*Applied Mathematics Research Centre, Faculty of Engineering and Computing, Coventry University, Priory Street, Coventry CV1 5FB, United Kingdom*
[2]*Key Laboratory of National Education Ministry for Electromagnetic Processing of Materials, Northeastern University, Shenyang 110004, Liaoning, China*

(Received 14 January 2013; accepted 22 April 2013; published online 24 May 2013)

An analysis of the successive regimes of the two-dimensional (2D) flow through a sharp 180° bend is performed by means of parametric numerical simulations where the Reynolds number Re and the opening ratio β (defined as the ratio of bend opening to the inlet width) vary in the respective ranges [0–2500] and [0.1–10]. In the outlet, the sequence of flow regimes is found to bear similarities with the flow behind a two-dimensional cylinder, despite being asymmetric by nature: when Re was increased, we found a laminar flow, then a flow with a first recirculation attached to the inside boundary, then one with a second recirculation attached to the top boundary. The onset of unsteadiness occurs through instability of the main stream and vortex shedding from the inside boundary. For $\beta \leq 0.2$, the flow is characterised by the dynamics of the jet generated at the very small turning part whereas for $\beta \geq 0.3$, it behaves rather like the flow behind an obstacle placed in a channel. This difference is most noticeable in the unsteady regimes where the vortex shedding mechanisms differ. While the former generates a more turbulent flow rich in small scale turbulence, the latter produces large structures of the size of the channel. In the turning part, further series of recirculation develop in each corner, akin to those identified by Moffatt ["Viscous and resistive eddies near a sharp corner," J. Fluid Mech. **18**, 1 (1964)]. For $\beta > 1$ corresponding eddies merge to form a series of alternately rotating recirculating cells, which occupy the whole width of the turning part. We find that for $\beta > 1$, the effective opening ratio β^*, which correspond to the area occupied by the mainstream while passing from the inlet to the outlet, tends towards a value of $\simeq$0.7. The combination of regimes in the outlet and the turning part yields a wealth of flow regimes, which open interesting possibilities to tailor the design of 180° bends to suit particular applications involving mixing, heat, and mass transfer. Selected 3D simulations show that with a few noticeable exceptions, 2D dynamics determine the main features of the flow (drag and recirculation length), even in a wide bend, while 3D structure tends to slow down the shedding mechanism. 2D simulations are thus not only relevant to configurations where the flow is expected to be 2D (thin bend, MHD flows), but also to 3D flows where they can predict some of the global flow features at a low computational cost. © *2013 AIP Publishing LLC*. [http://dx.doi.org/10.1063/1.4807070]

I. INTRODUCTION

Flows in bends present generic features that are common to a vast class of separated flows, such as flows around obstacles or behind a backward facing step. As such, their relevance extends well

a)Electronic mail: zhangl13@uni.coventry.ac.uk
b)Electronic mail: alban.potherat@coventry.ac.uk

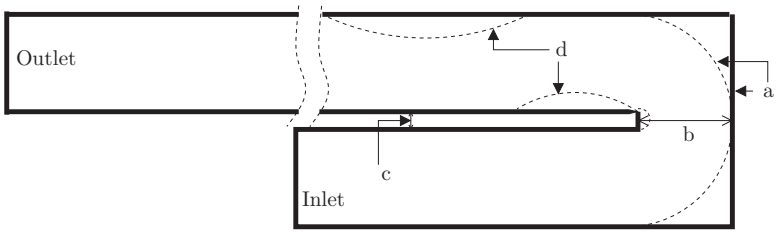

FIG. 1. Key points of 180° bend duct have been studied: turning part shape (a), turning part width (b), divider thickness (c), and secondary flow recirculations (d).

beyond that of their own dynamics.[1–3] Nevertheless, their study has been mainly driven by the need to optimise heat exchangers, many of which are made of a many-fold succession of sharp bends, mainly 180° bends, such as that sketched in Fig. 1. Blankets of nuclear fusion reactors, including the ITER prototype, are one recent and particularly complex example: these consist of an arrangement of bends in which a liquid metal flow transports away the heat generated in the fusion plasma. Obviously, the efficiency of this process is key to the efficiency of the whole reactor. Two of the difficulties to overcome are the very large head losses incurred as the flow passes through the blanket on the one hand, and to avoid the occurrence of dangerous hot spots where heat accumulates on the other hand.[4] Both are directly linked to the flow structure, which can be controlled by altering the inner or the outer geometry of the bend. This problem is a highly complex one involving the combined effects of the strong magnetic field that confines the plasma, convective heat, and mass transport as well as fluid dynamics. Nevertheless, even the presumably simpler question of how variations in the duct geometry affect the hydrodynamic flow regimes inside the bend is not known, even though the answering it would greatly help to optimise the blanket design. Our approach in this regard is rather modest: rather than solving a full problem, such as that of the fusion blanket, this paper is concerned with the precise determination of how changes in the bend geometry affect the nature of the purely hydrodynamic flow in a generic bend. In particular, we aim at characterising the dynamics of local recirculations and the onset of vortex shedding. Beyond their interest as generic separated flows, these structures directly determine head losses, heat transfer, and the occurrence of hot spots.

Unsurprisingly, the majority of studies concerned with the flow in 180° bends focuses on aspects related to heat transfer. Wang[5] studied the relationship between the turning part shape (Fig. 1(a)) and the heat transfer coefficient, to show that out of straight-corner (sharp bend) turn, rounded-corner turn, and the circular turn, the straight-corner turn produced the strongest turn-induced heat transfer enhancement. The width of the turning part of the sharp bend also influences the heat transfer coefficient (Fig. 1(b)): when the width changes from 50 mm to 30 mm, the mean Sherwood number (ratio of convective to diffusive mass transport) increases by 30%.[6] For a sharp bend duct, the maximum Nusselt number Nu (ratio of convective to conductive heat transfer) over the whole domain occurs in just downstream of the turning section.[7,8] The divider thickness (distance between the inlet top wall and the outlet bottom wall) also affects heat transfer process[9,10] (Fig. 1(c)): value of the dimensionless divider thickness (ratio of divider thickness to sum of inlet width and outlet width) around 0.25 produces the maximum total average Nusselt number. In practice, heat exchangers may contain more than one sharp turn section. Analyses of a three-pass passage show that heat transfer processes around the second sharp turn are virtually identical to those around the first one.[11] This confirms the relevance of single 180° bends to more realistic configurations.

The reasons behind these variations in heat transfer performances between different geometries originate in alterations of the flow patterns, and in particular of the dynamics of the recirculating flows that exist there[9] (Fig. 1(d)). The flow also becomes unsteady for large flow velocities, causing a dramatic heat transfer enhancement.[12] The dynamics of the recirculation that arises on the inside wall of the outlet part received most attention.[6] In a 180° sharp bend, the numerical simulations of Ref. 12 showed that its length increased with the Reynolds number in the range [50–600], until the flow becomes unsteady for Re $>$ 600. This behaviour resembles that of recirculations behind

obstacles[13] and downstream of a backwards facing step (BFS). In the latter configuration,[1] it was showed that the length of recirculation behind the step strongly depended on Re, with the flow becoming unsteady for Re $>$ 1200. The length increases linearly at low Re[3] and decreases in the unsteady regime, as for recirculations behind cylinders. Another feature common to the BFS and 180° sharp bend is the existence of a second recirculation downstream of the first one, but attached to the opposite duct wall. Downstream of a BFS, Ref. 3 found that it was displaced downstream as Re increased, because of the lengthening of the first recirculation. A similar secondary flow was noted in flows behind cylinders confined in a channel, at high blockage ratio.[14] Bouda *et al.*[15] and Schafer *et al.*[16] also found two recirculations behind a step with different directions for a turbulent wall jet flow. The 180° sharp bend, however differs from these two other configurations through the presence of two sharp corners in the turning part. In the vicinity of each of them, an infinite sequence of eddies of decreasing size and intensities when approaching the corner point always exist,[17–19] which were visualised in Mochizuki's experiments.[20]

From this short review, the influence of the duct geometry on heat transfer is well established and it operates by altering the flow regimes. Yet the precise effect of the geometry on the flow regimes themselves was never investigated systematically. Before characterising heat transfer in each flow regime, it is therefore necessary to determine the occurrence of these regimes and their hydrodynamic features when the geometry is altered. This shall be the focus of this paper: our analysis relies on a parametric numerical simulation based on an unsteady finite volume code. In the light of the aforementioned results on heat transfer in bends, we choose the configuration of a 180° sharp bend with a straight corner. We shall focus on the influence of the non-dimensional opening ratio β, between distance b in Fig. 1 and the inlet diameter. In order to cover an extensive range of parameters in terms of Reynolds number and β, we shall combine a detailed analysis of a purely two-dimensional (2D) flow with targeted numerical simulations of the full 3D problem. Beyond a great importance as an academic problem, understanding the 2D dynamics in detail is a crucial step in the analysis of this class of flow. First, it is directly relevant to a number of realistic configurations where the bend is very thin, such as laboratory experiments in Hele-Shaw cells[21,22] or soap films or in heat exchangers designed for small electronic components, and also to flows in high magnetic fields such as in ITER.[23,24] This class of flow can indeed exhibit boundary layer separation, instabilities, and turbulence with a clear two-dimensional dynamics.[25,26] Second, even in 3D flows, 2D and 3D dynamics are likely to coexist, as recently discovered in turbulent flows,[27] so not only do 2D simulations remain partly relevant to 3D flows but they are essential to understand the full dynamics. The goal of the subsequent 3D simulations will be to determine the limits of the strict validity of the 2D simulations and also to measure their relevance to the flow, when three-dimensionality is present. This will also serve as a first step for future work dedicated to aspects of the 3D flow.

The geometry and governing equations are given in Sec. II. The numerical setup is presented in Sec. III. We shall distinguish between the flow regimes in the outlet and in the turning part of the bend, which are, respectively, discussed in Secs. IV and V. 3D simulations are presented in Sec. VI.

II. PROBLEM GEOMETRY AND GOVERNING EQUATIONS

We consider an incompressible flow (density ρ, kinematic viscosity ν) in a 2D 180° sharp bend, represented in Fig. 2. The origin is placed at the middle of the inner wall of the turning part, with x coordinate along the inlet streamwise direction. The duct widths are a in the inlet and outlet and b in the turning part. c is the divider thickness and the lengths of the bottom and top boundaries are d and e, respectively. The ratios c/a and e/d are set to 0.04 and 3, while inlet and outlet, respectively, over $(d - b)/a = 15$ and $(e - b)/a = 30$ duct widths. β is defined as the ratio of b/a. It shall be referred to as the opening ratio, by analogy with the blockage ratio used for flows around obstacles.[23] Values of β in the range [0.1,10] are studied in order to investigate the influence of the geometry on the flow regimes. The flow dynamics are governed by the Navier-Stokes equations. Using a, the maximum inlet velocity, U_0, ρU_0^2, and a/U_0 as reference length, velocity, pressure, and time, the

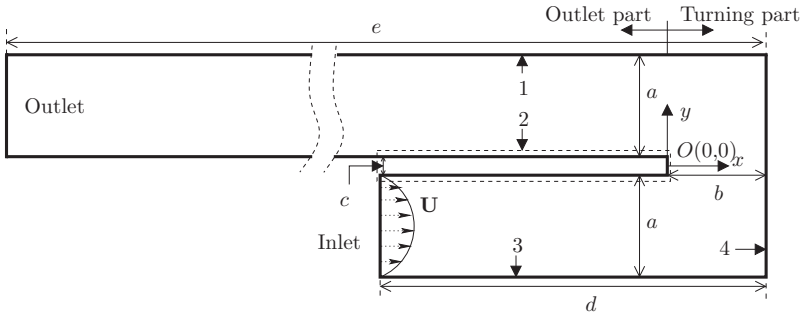

FIG. 2. The geometry of 180° bend duct for the whole domain. Boundaries are labelled as follows: 1, top boundary (T); 2, inside boundary (I); 3, bottom boundary (B); 4, end wall boundary (E).

non-dimensional equations can be written as

$$\partial_t \mathbf{u} + (\mathbf{u}\cdot\nabla)\mathbf{u} + \nabla p = \frac{1}{\mathrm{Re}}\nabla^2\mathbf{u}, \tag{1}$$

$$\nabla\cdot\mathbf{u} = 0, \tag{2}$$

where $\mathbf{u}$ is the non-dimensional flow velocity, p is the non-dimensional pressure, and $\mathrm{Re} = U_0 a/\nu$ is the Reynolds number. Along each of the walls B and E, a no-slip impermeability condition is imposed:

$$\mathbf{u} = 0. \tag{3}$$

A Poiseuille velocity profile is imposed at the inlet at $x = -0.9$:

$$\mathbf{u}_x(y) = [1 - (\frac{2(y+0.052)}{a})^2]. \tag{4}$$

The outlet boundary condition is designed so that the flow is back to streamwise invariance:

$$\mathbf{u}\cdot\nabla\mathbf{u}|_{x=-\frac{e-b}{a}} = 0. \tag{5}$$

At the same time, the length of the outlet was chosen to be sufficiently long for all vortical structures to have been dampened out before the flow reached the outlet, in order to avoid any upstream influence of this condition. In this regard, our choice of $\frac{e-b}{a} = 30$ results from an comfortable application to the bend of the length recommended for cylinder wakes,[28] taking the duct width as a reference length. It turned out *a posteriori* that the flow was indeed back to streamwise invariance well before reaching the outlet in all of our calculations.

Finally, as we shall see in Sec. III, we shall use a highly regular, structured mesh, together with the finite volume method, which can be artificially stabilising: in flows around cylinders this combination is known to exhibit transitions to recirculating or unsteady flows at higher critical Re than those experimentally observed. This behaviour can be compensated by introducing arbitrary velocity perturbations during a short initial period of the simulation. In the same spirit, as in the simulation of wakes, where it is customary to rotate the cylinder clockwise and counterclockwise, moving wall conditions are applied in the first stages of all calculations in near-critical regimes so as to artificially introduce some perturbative vorticity in the flow.[29] For instance, for instabilities originating near the inside boundary, the no-slip boundary condition on boundary (I) shall be replaced with

$$\mathbf{u} = \begin{cases} 0.1 & 0 \le t \le 1, \\ -0.1 & 1 \le t \le 2, \\ 0 & \text{otherwise.} \end{cases} \tag{6}$$

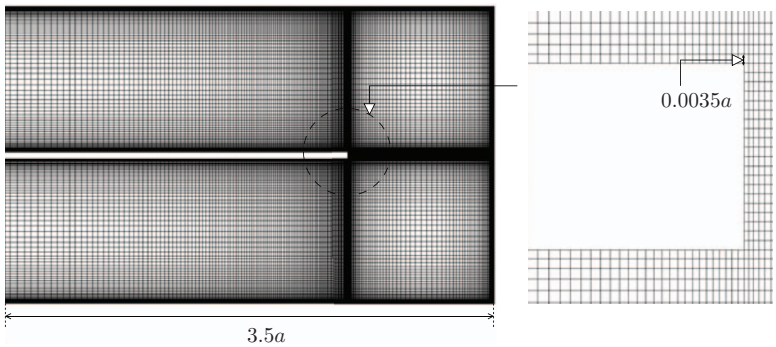

FIG. 3. Details of the meshes around turning part area.

A similar treatment was applied to boundary T, in near-critical conditions for flows subject to instabilities originating there.

III. NUMERICAL SETUP

Equations (1) and (2) are solved using the finite volumes method, with an unsteady solver. The spatial discretisation is of second order upwind and the time scheme is a second-order implicit pressure-velocity formulation. The velocity-pressure coupling is solved with the PISO algorithm.[30] Our code is based on the OpenFOAM framework, where these methods are implemented. It is essentially identical to its 3D counterpart, which we used and tested in Ref. 31. The mesh is fully structured and is refined in the vicinity of the walls (see Fig. 3). The size of the cell near all walls is about $0.0035a$. The detail of the meshes is given in Table I. During the simulations, the time step is constant and it must satisfy the Courant-Lewy-Friedrich condition, such that the maximum Courant number is always smaller than 1. For each fixed value of β, we first perform a simulation at $\mathrm{Re} = 1$. In subsequent simulations Re is increased in small steps, starting from the established state of the previous step. Values of β in the range [0.1, 10] are selected in order to investigate how the flow regimes depend on the geometry of the bend.

A first test is performed to determine the required number of cells in the mesh. We perform simulations for $\beta = 1$ at $\mathrm{Re} = 100$, for which the flow is steady and $\mathrm{Re} = 800$, for which the flow is unsteady. The drag coefficient C_d, the lift coefficient C_l, and Strouhal number $\mathrm{S_t}$ are, respectively, defined as

$$C_d = \frac{2\mathbf{F}\cdot\mathbf{e_x}}{\rho U_0^2 A}, \tag{7}$$

$$C_l = \frac{2\mathbf{F}\cdot\mathbf{e_y}}{\rho U_0^2 A}, \tag{8}$$

TABLE I. Characteristics of different meshes and C_d, $\mathrm{S_t}$, and U errors at $\mathrm{Re} = 100$ and 800 for $\beta = 1$.

Meshes	Mesh1	Mesh2	Mesh3	Mesh4	Mesh5
Total number of nodes	35 770	49 134	71 622	100 602	144 530
Number of nodes along boundary T	188	222	268	320	384
Number of nodes across the duct	48	56	68	80	96
$\epsilon_{\mathrm{S_t}} = \lvert 1 - \mathrm{S_t}(Mi)/\mathrm{S_t}(M5)\rvert$	7.11×10^{-1}	1.56×10^{-1}	1.45×10^{-2}	8.67×10^{-3}	...
$\epsilon_{C_d}^{100} = \lvert 1 - C_d(Mi)/C_d(M5)\rvert$	8.09×10^{-4}	5.23×10^{-4}	2.70×10^{-4}	1.27×10^{-4}	...
$\epsilon_{C_d}^{800} = \lvert 1 - C_d(Mi)/C_d(M5)\rvert$	1.74×10^{-2}	8.18×10^{-3}	3.55×10^{-3}	2.38×10^{-4}	...
$\epsilon_u^{100} = \sum \lvert u_{Mi} - u_{M5}\rvert / \sum \lvert u_{M5}\rvert$	6.73×10^{-3}	4.97×10^{-3}	3.13×10^{-3}	8.81×10^{-4}	...
$\epsilon_u^{800} = \sum \lvert u_{Mi} - u_{M5}\rvert / \sum \lvert u_{M5}\rvert$	5.84×10^{-2}	4.56×10^{-3}	3.42×10^{-3}	8.56×10^{-4}	...

$$S_t = \frac{f a \beta}{U_0}, \tag{9}$$

where **F** is the total force exerted by the fluid on the inside boundary, and A is the total surface of I and f is the frequency of vortex shedding. The latter corresponds to the peak of lowest frequency in the frequency spectrum found at Re = 800. We compute the errors $\epsilon_{\mathrm{S_t}}$, ϵ_{C_d}, and ϵ_u on $\mathrm{S_t}$, C_d, and U relative to the finest mesh M5 (see Table I, where the exact definition of these quantities is given). All three decrease when the total number of cells of the mesh increases, which shows good convergence. Thereafter, all the simulations are based on mesh M4, which ensures a good precision at a reasonable computational cost.

A further validation test was computed to investigate the accuracy of the numerical scheme for flows in bends. Chung[12] considered nearly the same geometry as in the present paper for $\beta = 1$, but with $c = 0.05$ instead of $c = 0.04$. They found that the flow became unsteady for $500 < \mathrm{Re} < 600$, which is consistent with our more precise result in the range $560 < \mathrm{Re} < 570$.

IV. FLOW IN THE OUTLET PART OF THE BEND

A. Flow regimes

1. General features

In all cases considered in this paper, the flow remains laminar in the inlet branch of the bend ($y < 0$, $x < 0$). In the whole of Sec. IV, we shall first focus on the dynamics of the flow in the outlet branch of the bend ($y > 0$, $x < 0$). Features of the flow in the turning part of the bend ($x > 0$) and its influence on the outlet flow shall be analysed in Sec. V.

For all opening ratios β, we were able to distinguish five different regimes as Re was increased, which we shall, respectively, refer to as regimes I, II, III, IV, and V (see Figs. 4–6 and 9). Re_1^c, Re_2^c, Re_3^c, and Re_4^c denote the first critical values of Re at which regimes II, III, IV, and V were, respectively, detected. The first three flow regimes are steady whilet subsequent regimes are unsteady. Up until unsteadiness is established, the flow follows the same scenario at all values of β, with some minor differences, whereas the evolution of the flow within regime IV and beyond exhibits fundamental differences, whether β is smaller or larger than about 0.3.

In regime I, encountered at the lowest Re, the flow is laminar and attached to the walls all the way through the bend. At very low Re, it is close to being symmetric about the $y = 0$ plane (see Figs. 4–6(a)), but when Re increases within regime I, streamlines are progressively displaced towards the upper part of the bend. More and more marked inflexion points around $x = -0.05$ to 0 can be noticed, and a region of low pressure develops downstream of the inside corner of the outlet. For $\mathrm{Re}_1^c < \mathrm{Re} < \mathrm{Re}_2^c$, the resulting adverse pressure gradient near the inside corner becomes strong enough to drive a return flow that leads to the appearance of a first recirculation $\mathrm{R_1}$ (Figs. 4–6(b)). This regime is defined as regime II and the corresponding flow is strongly reminiscent of the steady recirculating flow found behind an obstacle.[13] As Re increases within regime II, $\mathrm{R_1}$ lengthens and broadens, with direct consequence that the section of the bend available to pass the total flow rate is locally reduced. Downstream of the recirculation, the passage widens again so the pressure has a local minimum, as in a Venturi tube. This leads to the development of an adverse pressure gradient at the downstream edge of $\mathrm{R_1}$. For $\mathrm{Re}_2^c < \mathrm{Re} < \mathrm{Re}_3^c$, this adverse pressure gradient becomes strong enough to drive a second steady recirculation $\mathrm{R_2}$, which defines regime III (see Figs. 4–6(c)). Since $\mathrm{R_1}$ is attached to the inside wall, the adverse pressure gradient is stronger near the top boundary so the second recirculation develops there, rather than on the inside wall. In this flow regime, $\mathrm{R_1}$ and $\mathrm{R_2}$ coexist mostly in a steady state. Towards the end of regime III, however, oscillations of small amplitude appear that originate downstream of the recirculation in the main stream (about 3% of the max inlet velocity). The phenomenon is reminiscent of the oscillations that are detected in the tail of recirculations behind 2D obstacles, at slightly lower Re than the critical Reynolds number for vortex shedding. These fluctuations appear far downstream and propagate upstream as Re approaches the critical value for the onset of the next regime.

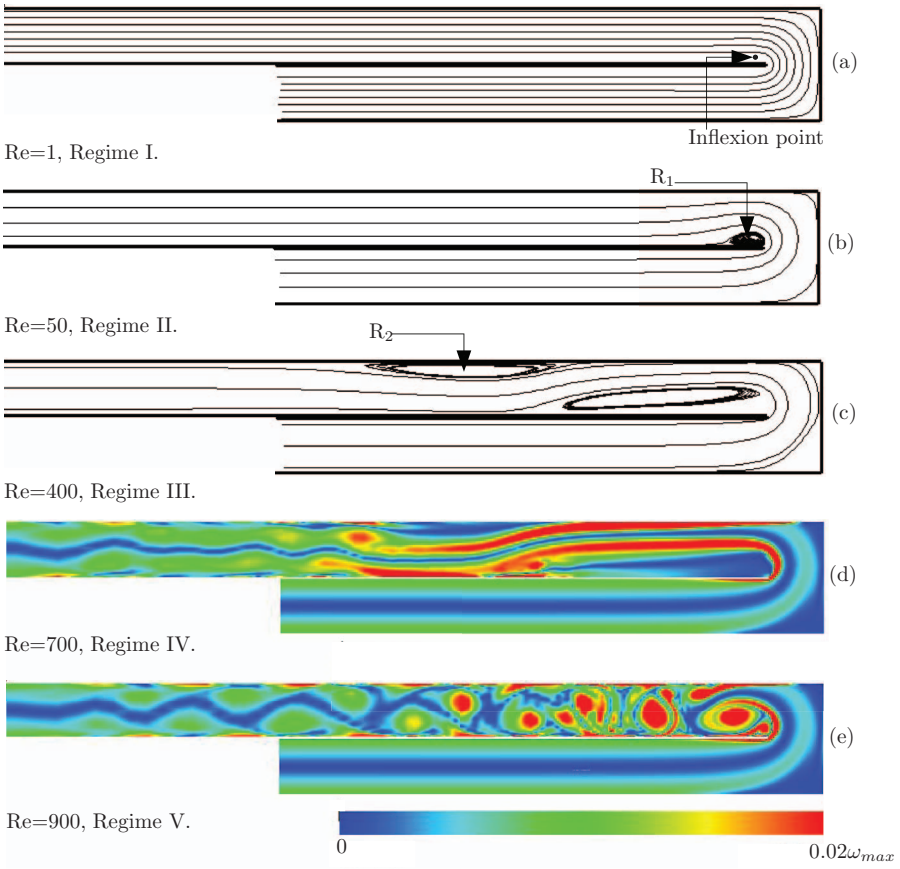

FIG. 4. Sequence of flow regimes in the outlet part for $\beta = 1$. (a)–(c) Streamlines of steady flow. (d)–(e) Snapshot of vorticity contours taken from the unsteady flow. The outlet part is only represented up to 15 duct widths for clarity, when the simulated domain extends in fact to 30 duct widths. ω_{max} stands for the dimensionless maximum vorticity which is normalised by U_0/a.

For $\mathrm{Re} > \mathrm{Re}_3^c$, a first kind of vortex shedding sets in, but unlike in the symmetric flows behind obstacles, it does not originate in the roll-up of the shear layers wrapped around any of the recirculations. Vortices of smaller scale are generated by the instability of the shear layer that carries the main stream between R_1 and R_2. This instability is of the Kelvin-Helmholtz type (see for instance Ref. 32) and takes place towards the downstream end of R_1. The unstable shear layer induces a collapse of R_2 to a much shorter length, but without any shedding associated to this structure. In this sense, R_2 remains a recirculation and does not become a vortex formation region, as recirculations behind cylinders do at the onset of vortex shedding. By contrast, R_1 remains essentially steady (see Figs. 4–6(d), and corresponding animations). Another distinctive feature of this regime is that in none of our simulations do flow quantities exhibit any simple periodic behaviour. Although a dominating mode could clearly be identified in the fluctuations of drag coefficient, the pattern of their variations is chaotic.

2. Influence of the geometry on regimes I–IV

The sequence of regimes described in Sec. IV A applies to all the values of β we investigated. Nevertheless, the flow within these regimes does exhibit some noticeable variations when spanning small to large values of β. Most noticeably, the internal structure of both recirculations is altered: at low values of β, the stream is carried around the first recirculation by a jet of typical size β. As the first recirculation lengthens in regimes I and II, it cannot expand transversally and adopts an increasingly elongated shape in the streamwise direction. As a consequence, closed streamlines

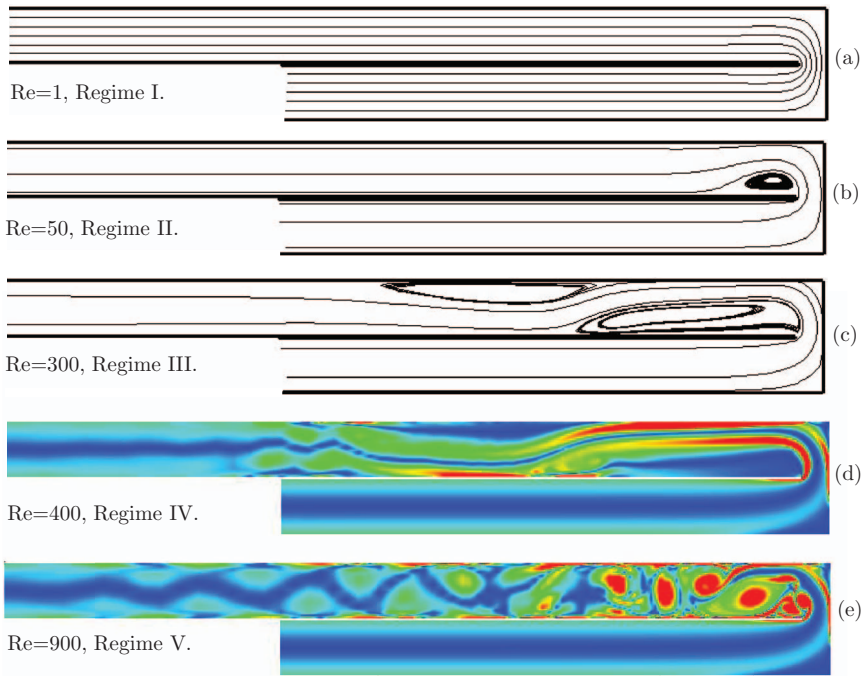

FIG. 5. Flow regimes in outlet part of bend for $\beta = 0.5$. See legend of Fig. 4. The outlet part is only represented up to 15 duct widths for clarity, when the simulated domain extends in fact to 30 duct widths.

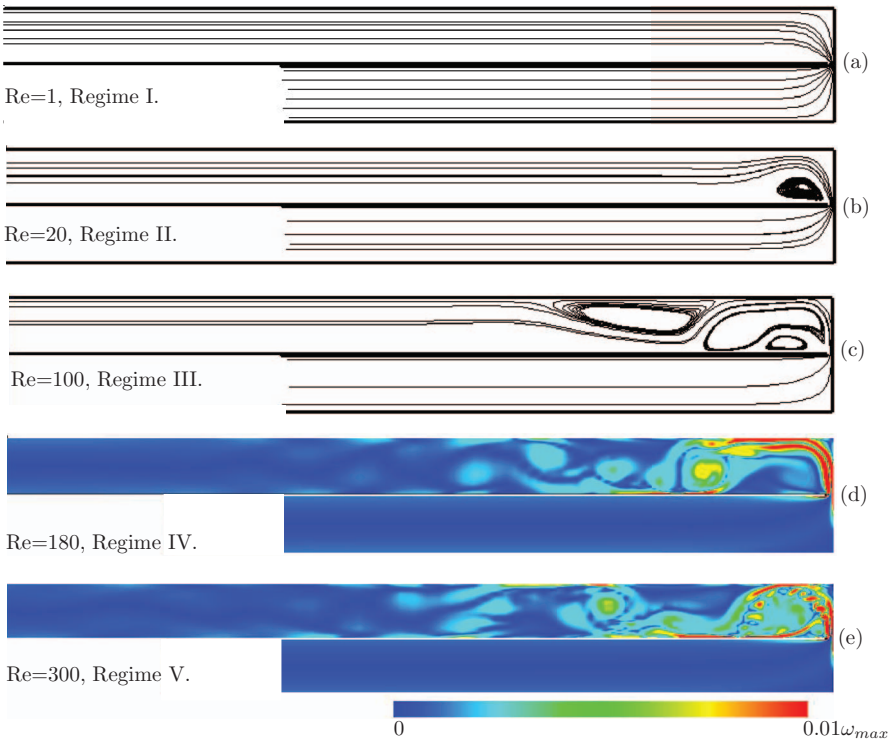

FIG. 6. Flow regimes in outlet part of bend for $\beta = 0.1$. The outlet part is only represented up to 15 duct widths for clarity, when the simulated domain extends in fact to 30 duct widths.

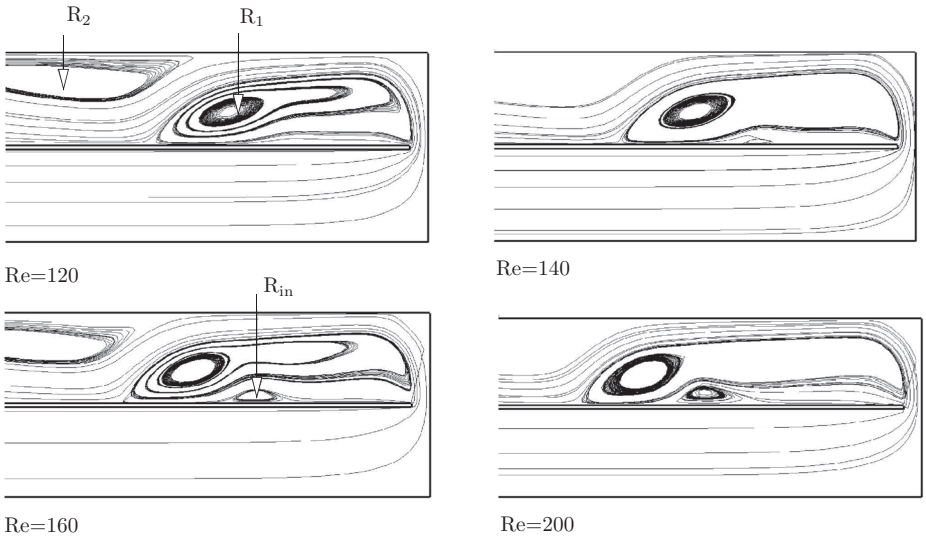

FIG. 7. Streamlines of the steady flow at $\beta = 0.2$, showing the stages of the development of the inside recirculation within R_1 at different values of Re.

concentrate near its downstream end, leaving a mostly stagnant zone on the upstream end. The proximity of this new intense vortex with the wall induces a counter-rotating vortex inside R_1, the stages of developments of which are shown in Fig. 7. For larger β, the constraint imposed by the upper wall on the development of R_1 only appears in the late stages of its lengthening, so the appearance of the inside recirculation is postponed to much higher values of Re. The variations of the corresponding critical Reynolds number Re^c_{in} are shown in Fig. 8. For $\beta > 1$, increasing the opening ratio does not change further the width of the main stream in the outlet so the confinement constraint on R_1 is essentially the same as for $\beta = 1$, consequently, $Re^c_{in}(\beta)$ does not vary further.

A somewhat similar influence of the boundaries on a recirculating flow was reported by Refs. 33–35: the authors noticed that a low pressure induced by a local suction through a channel wall led to the appearance of secondary vortices inside the main recirculation behind a backward-facing step.

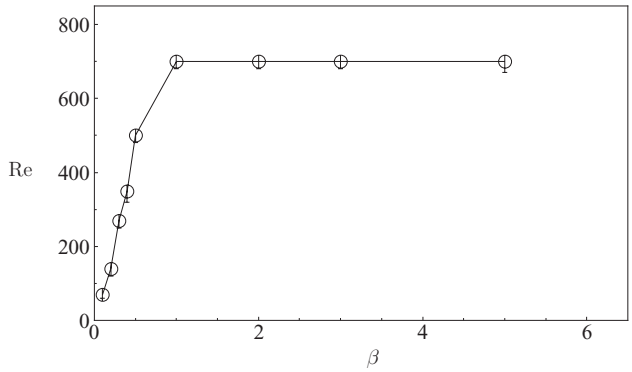

FIG. 8. Relationship between the critical Reynolds number Re_{in} for the appearance of the inside recirculation within R_1, and β.

3. Geometry-dependent unsteady regimes for $\beta \geq 0.3$

From regime IV onwards, a fundamental difference appears in the mechanisms that characterise subsequent regimes with $\beta \leq 0.2$ and those with $\beta \geq 0.3$. For $\beta \geq 0.3$, these unsteady regimes relate closely to those found in the wake of a 2D cylinder: as soon as Re exceeds Re_4^c, R_1 in turn collapses, but unlike R_2 it breaks up and sheds vortices (Figs. 4 and 5(e)). These are generated by the rolling of the outer shear layer that defined R_1. Consequently, their size is of the order of that of R_1 in the y direction, in contrast to vortices shed at the onset of regime III, whose size is determined by the thickness of the shear layer that separates R_1 and R_2, initially of the order of β (even though these tend to grow as they are released downstream). Again, unlike the von Karman street just after the onset of vortex shedding, the vortex street that results from the breakup of R_1 is chaotic and not periodic. This can be attributed to the presence of smaller vortices generated by the instability of the mainstream, as well as the strong influence of the channel walls. Strong geometric confinement indeed leads to counter-rotating secondary vortices being torn away from the wall boundary layers, which perturb the vortex street. The passing of these large vortices also results in the disappearance of R_2.

For $\beta \leq 0.2$, the flow becomes quickly turbulent right after the onset of unsteadiness. This renders the identification of flow structures significantly more difficult than for $\beta \geq 0.3$. Regime V appears at $\mathrm{Re} = \mathrm{Re}_4^c$, when R_1 collapses, as for $\beta \geq 0.3$. On these grounds, we shall also label as V this new regime. Yet, its features exhibit three major differences with regime V for $\beta \geq 0.3$: first, no rolling up of the shear layer around R_1 occurs. Instead, the layer undergoes an instability of the Kelvin-Helmholtz type as did the mean stream in regime IV. Since the layers around both recirculations essentially form one structure, this translates into Kelvin-Helmholtz vortices being generated right in the vicinity of $x = 0$, rather than further downstream as in regime IV: the vortex generation mechanisms are therefore radically different in regime V for $\beta \leq 0.2$ and $\beta \geq 0.3$: instead of the large vortices of the size of R_1 shed for $\beta \geq 0.3$, small ones of typical size β shed for $\beta \leq 0.2$. The second major difference is that the recirculating region is not completely destroyed. The strong inner vortex that formed inside R_1 in the steady regime is brutally displaced to become attached at $x = 0$, and essentially constitutes what remains of R_1 in this regime. It transports Kelvin-Helmholtz vortices generated near point O, thus generating the highly identifiable "wheel" pattern that is visible in Fig. 6(d). In other words, rather than the collapse of the entire recirculation, the onset of regime V corresponds to the collapse of its inner stagnant region. Third, the small shed vortices squeeze under R_2, which therefore survives the collapse of R_1. The flow being turbulent, the internal structure of R_2 however becomes very complex: it is dominated by an intense vortex near its downstream edge which results from the same mechanism as that present inside R_1 during the steady regime (see Sec. IV A 2).

Finally, it should be noticed that our simulations do not allow us to conclude as to whether the important differences which we noticed between the regimes of "jet flow" at $\beta \leq 0.2$ on the one hand and those reminiscent of the wake behind an obstacle in a channel at $\beta \geq 0.3$ on the other hand, reflect a bifurcation, or whether the flow smoothly evolves from one scenario to the other.

4. Phase diagram

The variations of $\{\mathrm{Re}_i^c\}_{i\in(1,2,3,4)}$ with β are summarised in the phase diagram in Fig. 9, along with the regimes discussed in this section and in Sec. V, which deals with the turning part. It can be seen that Re_1^c is only weakly sensitive to β when $\beta < 0.3$, whereas the value of Re_1^c increases rapidly with β when $0.3 < \beta < 1$. For $\beta > 1$, Re_1^c becomes weakly dependent on β and the geometry again. By contrast, the curves for Re_2^c, Re_3^c, and Re_4^c only exhibit two distinct regions: one where Re_2^c, Re_3^c, and Re_4^c are sensitive to β ($\beta < 1$), and the other one where they are both robust to the variations of β ($\beta > 1$). This can be understood as follows: the "robust" region at $\beta < 0.3$ corresponds to the jet flow regimes identified previously, where the mainstream is injected in the outlet through a small aperture: in the bend, the flow direction is almost parallel to $\mathbf{e}_y$ and impacts the upper outside wall where it turns brutally along $\mathbf{e}_x$. Progressively increasing β therefore modifies the flow near the top boundary directly, but has little influence on the region near the inside boundary where R_1 appears. This explains why Re_1^c varies little in this range of parameters. For $0.3 < \beta < 1$, the main flow

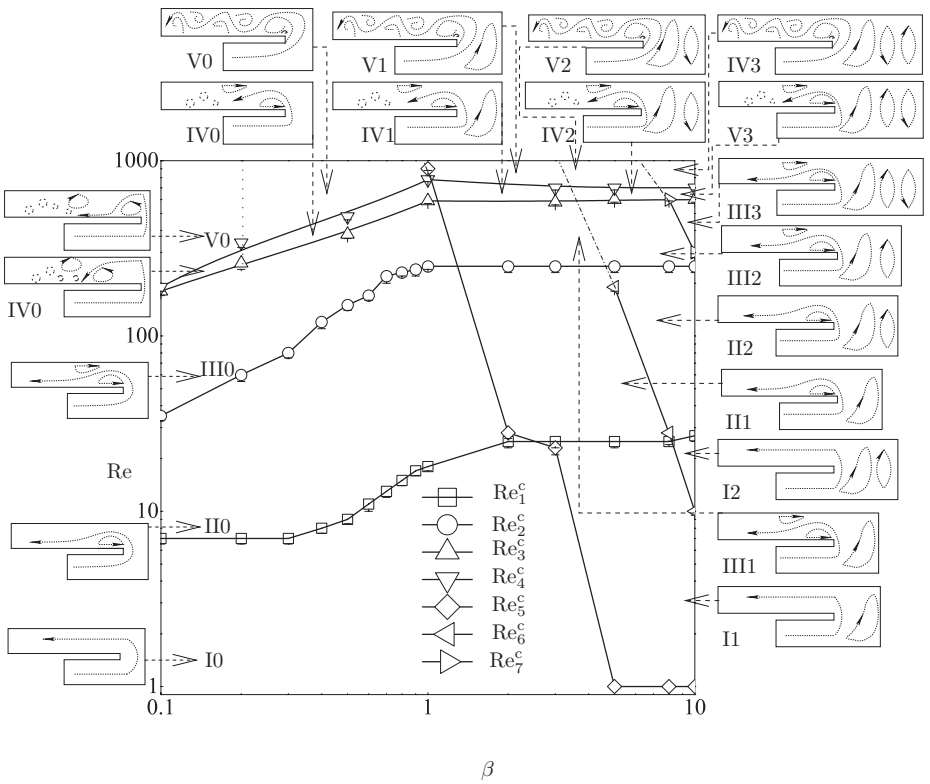

FIG. 9. Phase diagram of 180° sharp bend: flow regimes are labelled by Roman characters followed by numbers. These, respectively, stand for the outlet flow regimes and the number of merged recirculations in the turning part section. A schematic representation of each combined flow regime is given for each distinct region of the phase diagram. Error bars span the interval between numerical simulations showing the "last stable" and those showing "first unstable" one.

direction gradually changes along $\mathbf{e}_y$ within the bend, and starts to affect the flow near the inside boundary. In this regime, Re_1^c becomes therefore sensitive to β. When $\beta > 1$, the bend end wall is far from the inside corner and influences the flow there very little. Consequently, Re_1^c becomes robust to β again, as do Re_2^c, Re_3^c, and Re_4^c for the same reason. The cause of the dependence on β of Re_2^c for $\beta < 0.3$ is somewhat indirect: in jet flow regimes, for $\mathrm{Re} > \mathrm{Re}_1^c$, mainstream consists mainly of a jet of width of the order of β, which circulates around the first recirculation. Increasing β increases the jet section, and thus reduces the adverse pressure gradient associated to the stream widening behind the first recirculation. This effect becomes visible when comparing Figs. 4(c), 5(c), and 6(c). Higher values of Re must therefore be reached to trigger the appearance of the second recirculation, when β increases. Similarly, the dependence of Re_3^c and Re_4^c on β for $\beta < 0.3$ can be attributed to the alteration of the jet thickness too.

B. Dynamics of the outlet recirculation

1. General features

We shall now explore the dynamics of the recirculation regions which characterise the five regimes found in the outlet branch. Since all recirculations are attached to walls, we use the points where the friction force $\rho\nu\partial_y u_x$ changes sign on the upper and lower outlet walls to pinpoint the exact locations of the separation and re-attachment points where recirculations begin and end. These are schematically represented in Fig. 10, for R_1, R_2, and R_{in} and The variations of these locations with Re are represented in Fig. 11 for several values of β.

For all values of β, the length L_1 of R_1 increases linearly with Re in the first stages of regime II, again a similar behaviour to that of the steady recirculations observed behind 2D obstacles. Unlike

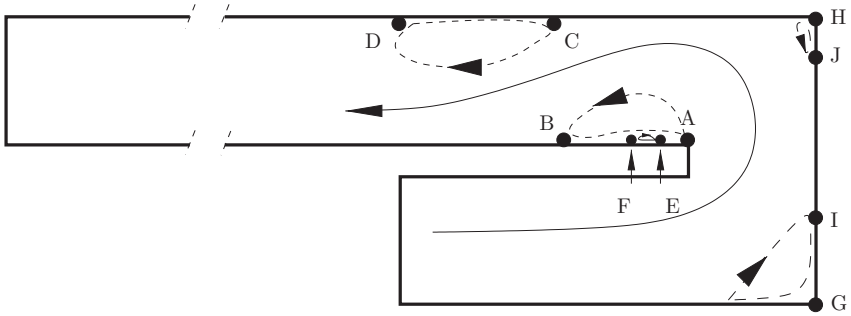

FIG. 10. Sketch of separation and re-attachment points defining the locations of all recirculations.

them, however, the length saturates, and more so when R_2 is present. The lengthening is due to the friction exerted by the main stream. Because of the confinement, however, the adverse pressure gradient caused by the widening of the mainstream just downstream of the main recirculation opposes further lengthening. This effect is reinforced by the appearance of R_2, which incurs a much larger adverse pressure gradient. The length L_2 of R_2 follows similar dynamics. Remarkably, its separation point is hardly displaced in the whole of regime III, most likely because it is determined by the length of R_1, which varies little itself throughout this regime, for the reasons outlined above. As vortices disrupt the outer shear layer that surrounds R_2 (for $\mathrm{Re} \geq \mathrm{Re}_3^c$), the time average of its length $\langle L_2 \rangle$ collapses, as in flows behind obstacles. The collapse of R_2 slightly releases the confinement of the main stream, downstream of R_1, so the latter sees its length slightly increases at $\mathrm{Re} \simeq \mathrm{Re}_3^c$, and remains practically constant over $\mathrm{Re}_3^c < \mathrm{Re} < \mathrm{Re}_4^c$. At $\mathrm{Re} = \mathrm{Re}_4^c$, either vortex shedding starts ($\beta \geq 0.3$), or Kelvin-Helmholtz vortices are released near point O ($\beta \leq 0.2$). In both cases, R_1 collapses and so does the time average of L_1, $\langle L_1 \rangle$.

2. Influence of the geometry on the recirculation length

The most obvious effect of varying β on this picture is that steady recirculations and unsteady vortex formation regions are overall shorter at smaller β. This can be seen in Fig. 11, and also on the streamlines and vorticity contours represented in Figs. 4–6. Furthermore, the range of Re over which R_2 remains steady and keeps a practically constant length shrinks when β is reduced, to the point of practically disappearing at $\beta = 0.1$ (see Fig. 11).

Further insight on the role of the geometry is gained by plotting L_1 and L_2 against critical parameters for the onset of regimes II and III, respectively (see Fig. 12). Critical parameters are defined as $r_1 = \mathrm{Re}/\mathrm{Re}_1^c - 1$ and $r_2 = \mathrm{Re}/\mathrm{Re}_2^c - 1$. For R_1, the curves collapse to $L_1 \simeq r_1^{0.3}$ over the interval $0 \leq L_1 \lesssim 1.4$, indicating that increasing β in this regime mainly results in postponing the appearance of the R_1, without affecting its overall dynamics. For $3 \lesssim r_1 \lesssim 20$, the curves separate, as R_1 lengthens more noticeably with r_1 at higher values of β. In this range, R_2 is present and influences the development of R_1. Since this effect is not controlled by r_1 anymore, it appears that the variations of opening ratio β do not influence R_1 and R_2 in the same way, a point which already reflected on the difference in the variations of Re_1^c and Re_2^c noted in Sec. IV A 4. The sharp drop in all curves over the range $20 \lesssim r_1 \lesssim 80$ corresponds to the onset of regimes V ($\mathrm{Re} = \mathrm{Re}_4^c$), when R_1 collapses, as discussed in Sec. IV B 1.

By contrast, L_2 does not obey any universal behaviour controlled by r_2. For $\beta \geq 0.3$ (channel regimes), L_2 increases with r_2 when $r_2 < 1$ and a first drop of L_2 occurs in the range $1 < r_2 < 2$, which corresponds to the onset of unsteadiness. A second, sharper drop is visible at the onset of vortex shedding from R_1, following which $\langle L_2 \rangle$ remains very low as R_2 is essentially destroyed. The residual value can be attributed to the presence of vortices forming on the upper wall near $x = 0$, under the influence of vortex formation region that replaces R_1. For $\beta \leq 0.2$ (jet regimes), L_2 increases with r_2 and drops at $r_2 = 2.3$ and 3.1 for $\beta = 0.2$ and $\beta = 0.1$, respectively. As previously, this drop is caused by fluctuations at the onset of unsteadiness, that cause R_2 to collapse. Unlike for larger values of β, however, this is followed by a new increase in $L_2(r_2)$ over a small interval. The

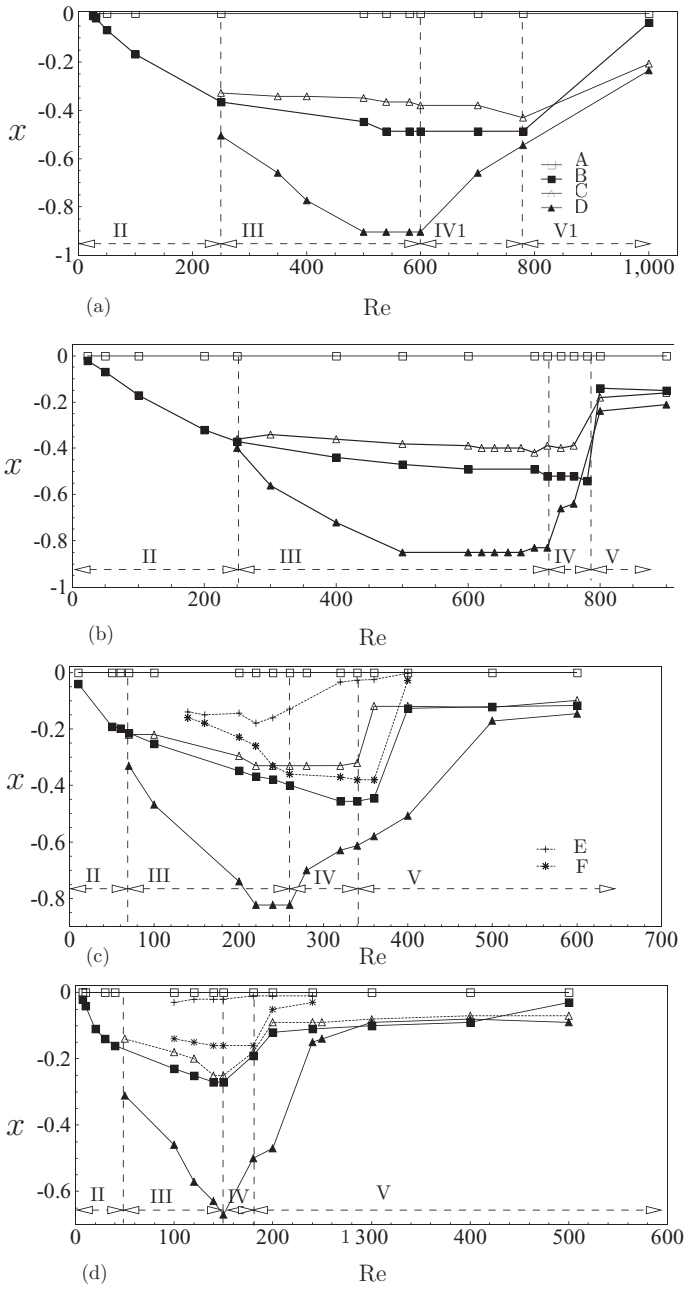

FIG. 11. Time average of separation and re-attachment points in the outlet branch of the bend vs. Re. (a) $\beta = 2$, (b) $\beta = 1$, (c) $\beta = 0.2$, and (d) $\beta = 0.1$.

collapse of R_1 causes this phenomenon, as illustrated in Fig. 13. We noticed that as R_1 collapses for $\beta \geq 0.3$, the whole of R_2 was displaced to follow the position of the re-attachment point that marks the end of R_1. For $\beta \leq 0.2$, by contrast, only separation point C recedes when this happens, while re-attachment point D essentially remains in the same position, thus causing a lengthening of R_2 by an amount equal to that by which R_1 shrinks. Further in regime V, $L_2(r_2)$ decreases smoothly.

An alternate way to appraise how the geometry affects the recirculations is to examine how their respective lengths vary when Re is held constant but β varies. This can be seen in Fig. 14. The values $\mathrm{Re} = 50$ and $\mathrm{Re} = 250$ are selected for R_1 and R_2, respectively, to ensure that the flow remains within the same regime at a given value of Re (respectively, regimes II and III for $\mathrm{Re} = 50$

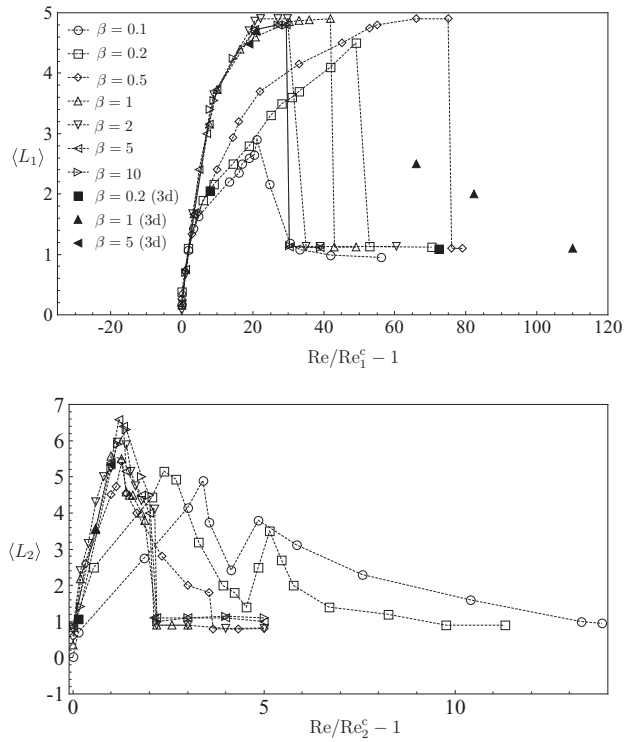

FIG. 12. Variations of recirculation lengths $\langle L_1 \rangle$ (top) and $\langle L_2 \rangle$ (bottom) against their respective critical parameters for several fixed values of β.

and $\mathrm{Re} = 250$). Both curves exhibit similar behaviour: L_1 first increases with β for low β ($\beta \leq 0.2$) and then decreases ($0.3 < \beta < 1$). The increase in the jet regimes reflects the fact that the growth of R_1 is governed by the scale of the mainstream jet β. The decrease of $L_1(\beta)$ for $\beta \geq 0.3$ is due to the sharp increase of $\mathrm{Re}_1^c(\beta)$ in this range. Indeed, increasing β in this range places the flow in a

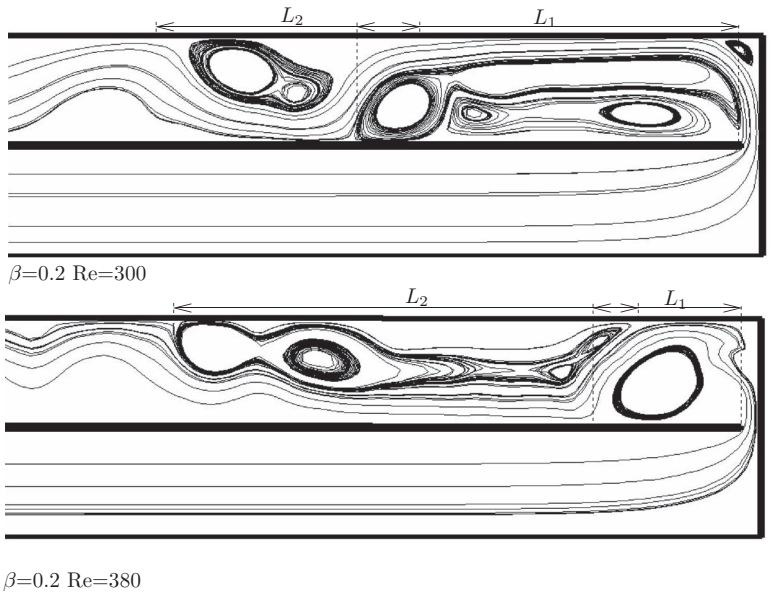

FIG. 13. Sketch of L_1 and L_2: just before (top) and just after (bottom) the collapse of R_1 (top), in the sense of increasing Reynolds.

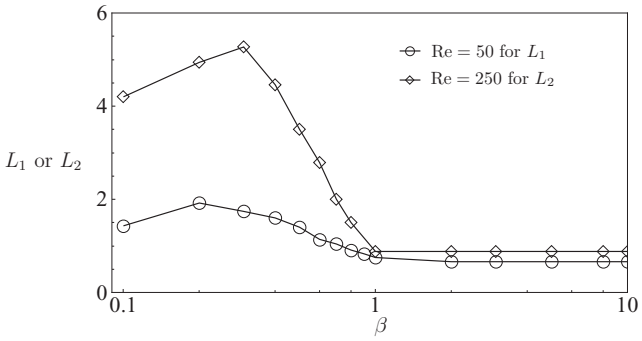

FIG. 14. Variations of the length of the steady and unsteady recirculations with β for fixed values of Re.

much less supercritical regime, where L_1 is significantly reduced. In the last part of the diagram, L_1 then becomes practically independent of β for $\beta \geq 1$. This is a consequence of the duct profile for $x \leq 0$ becoming essentially independent of the bend geometry in this range of parameters. Similar dynamics explain the variations of $L_2(\beta)$ in regime III at $Re = 250$.

C. Flow coefficients

1. Drag and lift coefficients

An important aspect of flows in bends from the engineering point of view is the feedback force of the flow onto the structure. Not only does it set constraints in design, but it also provides a convenient way to diagnose the flow, provided the measure of these forces can be linked back to the flow dynamics. Having determined the dynamics of the flow in the outlet part, we shall now establish this link. To this end, we analyse the dependence of the drag and lift coefficients, C_d and C_l, with the control parameters Re and β. These are defined by (7) and (8) for the inside boundary, which is akin to a 2D obstacle, for which these quantities are usually defined.

These are better understood recalling that the total drag and lift forces on the inside boundary both include a contribution due to viscous forces and one due to pressure forces. Both act on the inlet and outlet parts of the inside boundary, and also on the much smaller part in the turning area of the bend. We shall refer to the latter as the IVS (inside-vertical surface). Fig. 15 summarises the different components of these forces. Figs. 16 and 17 show the variations of C_d and C_l with Re, for fixed β. These share approximately the same features at all values of β: C_d first increases, then decreases past a peak value, whereas C_l decreases to a minimum in steady regime, then increases before dropping a little at the onset of unsteadiness. This can be understood as follows: for values of Re of a few units, the flow is almost symmetric about the $y = 0$ plane so the values of C_d and C_l result mostly from the force exerted on the IVS. The vertical friction and horizontal pressure forces

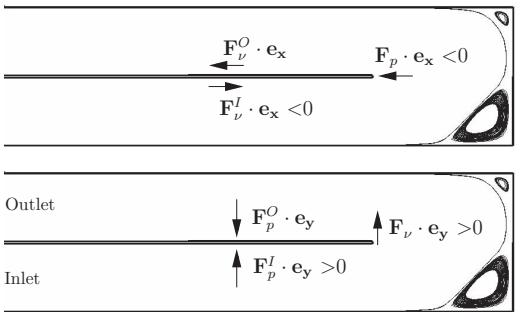

FIG. 15. Force direction on inside boundary: C_d (up) and C_l (bottom).

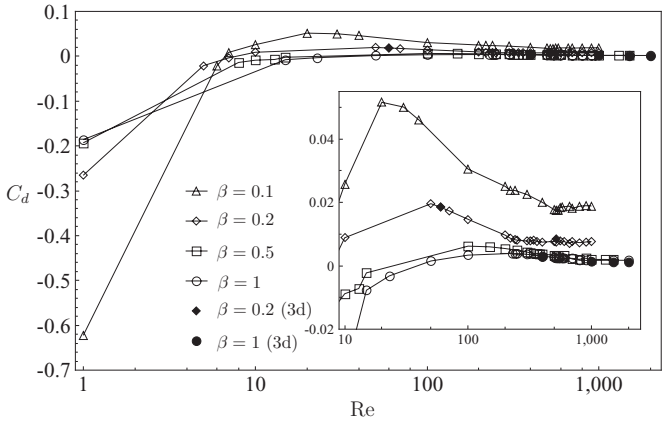

FIG. 16. The relationship between C_d with Re of inside boundary.

there, respectively, incur a positive lift and a negative drag. As Re increases, the flow progressively looses its symmetry and tends to turn closer to the upper right corner of the bend. This reduces the curvature of streamlines near O, and reduces the pressure deficit there. Furthermore, the main stream thus enters the outlet part with a small incidence with respect to the inside boundary, that incurs increased pressure and drag on it. Both these effects are enhanced as Re increases and, since they tend to oppose the force on the IVS, C_d and C_l, respectively, increase and decrease towards 0.

The appearance of R_1 mostly affects C_d, as it introduces a region of positive drag. This effect is however partly counteracted by the increased incidence of the flow onto the inside boundary just downstream of the recirculation. The consequence is that C_d becomes positive for Re slightly larger than Re_1^c, and reaches a maximum as the length of R_1 saturates. Subsequently, both the negative friction outside R_1 and the positive friction inside it increase with the flow intensity. Nevertheless, the flow incidence downstream of R_1 is increased by the presence and the growth of R_2, and thereby the negative friction there, so that C_d overall decreases. The appearance of R_1 is of little consequence on the variations of C_l, as the pressure drop inside it is mostly balanced by the increased pressure due to the expansion of the main stream downstream of R_1. The appearance of R_2, on the other hand, precedes (in the sense of increasing Re) a minimum in C_l. As R_2 grows, so does the region of low pressure, the outlet where the main stream is squeezed and accelerated against the inside boundary. This alteration in the flow geometry therefore induces a Venturi effect which is responsible for the increase in C_l past the minimum.

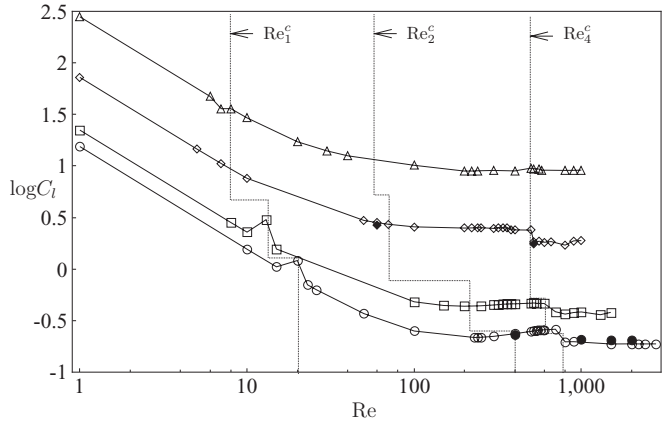

FIG. 17. The relationship between C_l with Re of inside boundary.

At the onset of regime V, the important distinction between jet regimes ($\beta \leq 0.2$) and channel regimes ($\beta \geq 0.3$) reflects mostly on the evolution of C_l: in the latter, R_1 collapses and is replaced by a vortex formation region: the associated low pressure region above the inside boundary disappears, and the lift thus drops. For $\beta \leq 0.2$, by contrast, a large recirculating flow remains when R_1 collapses, that maintains a low pressure locally. The corresponding change in C_l is hardly noticeable.

With this noticeable exception, the variations of β affect the relative importance of these effects, rather than the global picture. For small values of β, the flow passes through a narrow gap in the turning part so the forces on the IVS are high. As β is increased, the flow in the turning part is displaced towards the end wall, and both viscous force and pressure force on the IVS correspondingly decrease. The values of C_d and C_l therefore decrease with β, particularly so at low Re where the influence of the turning part is more important. At lower values of β, the region where the flow changes direction is partly inside the outlet (see Fig. 6). The consequences are that the flow enters the outlet with a stronger incidence and incurs a stronger pressure drop along R_1. Since these two effects drive the variations of C_d and C_l, these are amplified. In particular, the peak value of C_d that follows the onset of the R_1 is more pronounced at a low value of β (see the magnified part of Fig. 16, middle).

2. Strouhal number

The Strouhal number was defined by Eq. (9). Since it characterises unsteady flows, we shall discuss its dependence on the Reynolds number separately for jet and channel regimes. Fig. 18 shows the relationship between S_t and Re for $\beta = 1$ and $\beta = 0.5$, i.e., both in "channel" regime. Both curves follow the same tendency, with a sharp increase in regime IV, a slower increase in regime V followed by a maximum. In regime IV, smaller scale vortices are generated in the main stream between R_1 and R_2. The corresponding sharp increase of $S_t(Re)$ reflects the intensification of shedding that follows the onset or regime IV. This effect is favoured by the growth of both recirculations, which induces a thinning of the main stream, and intensify the shear where the Kelvin-Helmholtz instability occurs. At the onset of regime V ($\mathrm{Re} = \mathrm{Re}_4^c$), larger structures shed from R_1 with a slower dynamics. Consequently, $S_t(Re)$ continues to increase, exactly as it does at after the appearance of a Von Karman street in the wake of 2D obstacles, but along a significantly smaller slope. Remarkably the shedding frequency at the onset of regime V matches that of smaller vortices in regimes IV just before the onset, so that the curve $S_t(Re)$ does not seem to exhibit any discontinuity. The maximum of $S_t(Re)$ occurs well into regime V and can be attributed to the influence of the channel walls: Fig. 19 shows two snapshots of vorticity contours near (Re = 1500) and well past the maximum (Re = 2000) of S_t for $\beta = 1$. At Re = 1500, although some secondary vortices are generated at the wall in the wake of the main shed vortices, the vortex street flows downstream relatively unaltered. At Re = 2000,

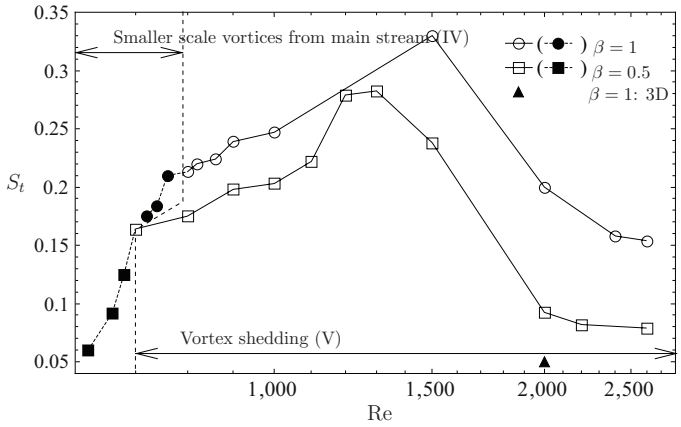

FIG. 18. The relationship between S_t with Re of $\beta = 1$ and $\beta = 0.5$. Black and white symbols, respectively, refer to shedding in regimes IV and V.

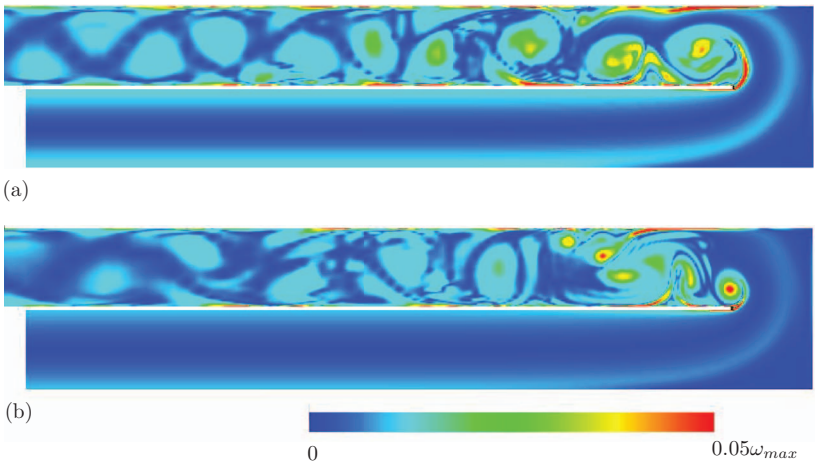

FIG. 19. Snapshot of vorticity contours taken from unsteady flow for $\beta = 1$: (a) At Re = 1500, near the Maximum of $S_t(Re)$, the vortex street is still well defined; (b) at Re = 2000, past the Maximum of $S_t(Re)$, the interaction with the walls destroy the vortex street.

by contrast, strong vorticity plumes and secondary vortices are torn away from the wall boundary layers. These impede the progression of the main shed vortices, and even their formation near $x = 0$. As this effect is amplified at higher Reynolds numbers, the S_t drops correspondingly. Once the vortex street is destroyed, it remains constant at a low value. The flow is then strongly turbulent, and it is more difficult to distinguish a dominating frequency. Similarly, experiments and numerical simulations[23,36] showed that in the wake of a 2D obstacle in a channel, the Von Karman vortex street could also destroyed by secondary vortices. The onset of this regime was also characterised by a maximum in $S_t(Re)$.

The variations of S_t(Re) for the jet flow (here $\beta = 0.2$) are depicted in Fig. 20. The shape of the curve at $\beta = 0.2$ is similar to those at $\beta = 1$ and $\beta = 0.5$, but for two noticeable features: first, there is no brutal change in the slope of S_t(Re) at the onset of regime V and second, the values of S_t are much higher at $\beta = 0.2$. The continuity in the slope at Re = Re_5^c stems from the fact that in jet regimes, the shedding mechanism in regime V is essentially the same as in regime IV. Small vortices are generated with fast dynamics in both regimes and the values of S_t reached in regime V are consequently much higher than those at $\beta \geq 0.3$, which are dominated by larger, slower structures. As for $\beta = 0.5$ and $\beta = 1$, an obvious drop in S_t can be seen (here for Re > 600), which, here again, can be attributed to the influence of the walls.

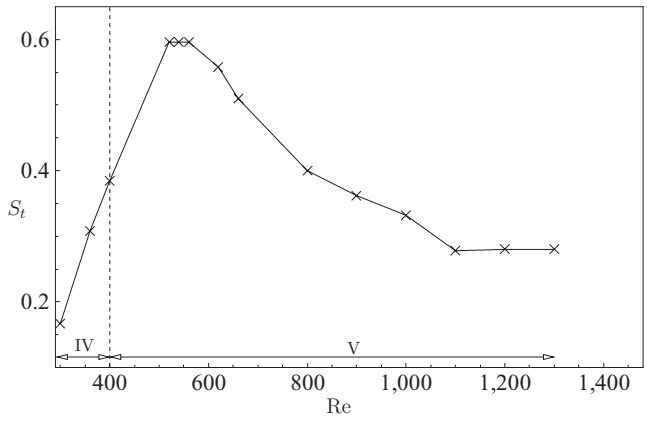

FIG. 20. The relationship between S_t with Re of $\beta = 0.2$.

V. FLOW OF TURNING PART OF THE BEND

A. Flow regimes

We shall now analyse the turning part of the bend, which corresponds to the region $x > 0$, where the flow changes direction from the inlet towards the outlet. The dynamics of this region is dominated by the presence of the two corners. According to Ref. 18, an infinite sequence of vortices of alternate spin exists near each of them, even for arbitrary low Reynolds numbers. Their size and intensity decrease geometrically as the distance to the corner decreases. For finite but low Reynolds numbers, the out-most vortex gives birth to a noticeable but small recirculation in each of the corners. We shall denote these, respectively, R_1^U and R_1^L for the upper and the lower corner. When Re is increased, asymmetry develops between the two corners recirculations as the flow is displaced towards the upper corner. This can be seen in Fig. 21. The length of R_1^U in the y direction, measured along the side wall, increases correspondingly slower with Re than that of R_1^L. This reflects on the position of the re-attachment points on the side boundary, whose evolution with Re is depicted for several values of β in Fig. 22. Unlike for the outlet flow, the succession of flow regimes in the turning part of the bend depends strongly on the value of β, right from low values of Re. In all simulations at $\beta \leq 1$, we observed that when Re is further increased, both R_1^U and R_1^L continue to grow but eventually saturate (around $\mathrm{Re} = 400$ for $\beta = 0.2$ and $\mathrm{Re} = 800$ for $\beta = 0.5$). For $\beta \simeq 1$, a second steady regime exists as the growth of R_1^U and R_1^L leads to their merging at critical Reynolds number $\mathrm{Re} = \mathrm{Re}_1^M$. Examples of flows in this regime are depicted in Fig. 21. The reason for the absence of merging at low β is that the proximity of the inside wall pinches the flow near the middle of the side wall. This imposes a local pressure minimum that prevents the build-up of the adverse pressure gradient that is necessary to drive a return flow along the end wall. In all cases, as Re is increased, more and more of the initially infinitesimal corner vortices grow to our finest mesh size and appear as detectable recirculations along the end wall. We shall denote these as R_i^U and $R_i^L / i \in \mathbb{N}$. Unlike the sequence of recirculations that develop on alternate walls of the outlet, though, these do not appear at a critical value of Re, as they are all already present at arbitrarily small values of Re, even though they may remain below the local mesh size.

For $\beta \geq 5$, further pairs of recirculation R_i^U and R_i^L merge so the turning part of the bend is progressively filled with a sequence of alternately rotating, steady recirculations that extend between the top and bottom walls. Fig. 21 shows an example where two counter-rotating recirculations are present for $\beta = 5$ and $Re = 200$. The merging of pair R_i^U and R_i^L occurs at a critical Reynolds number Re_i^M, which decreases with β. The variations of $\mathrm{Re}_i^M(\beta)$ are represented on the phase diagram (Fig. 9). Since they intersect the curves Re_i, the combination of the dynamics of the turning part of the bend and of those of the outlet defines a wealth of regimes corresponding to different flow configurations in either parts of the bend.

B. Effective turning dimension of 180° sharp bend

As β increases, the main flow could have been expected to change direction from the inlet (x direction) to outlet ($-x$ direction) over an extended area. It was established in Sec. V A, however, that instead, one or several recirculations appear there, that effectively reduce this area and push the main stream back into the $x < 0$ direction. This implies that only a fraction of the turning part area of the bend is effective in passing the main stream. To quantify this phenomenon, we define b^*, the effective width of the main stream across the bend section at $y = 0$. Accordingly, β^* is defined as

$$\beta^* = \frac{b^*}{a}. \tag{10}$$

Fig. 23 shows the relationship between β^* and Re for several fixed values of β. In the absence of recirculation extending over the whole turning part of the bend, the main stream reaches the outer vertical wall and so $\beta^* = \beta$. For $\beta \leq 1$, this remains the case at all Reynolds numbers. For $\beta \geq 2$, β^* remains equal to β at low values of Re. It then drops sharply as soon as the first pair of corner recirculations merge to extend along the full height of the turning part. As Re is increased, the flow intensity in the recirculation increases, and the curvature of the streamlines there diminishes.

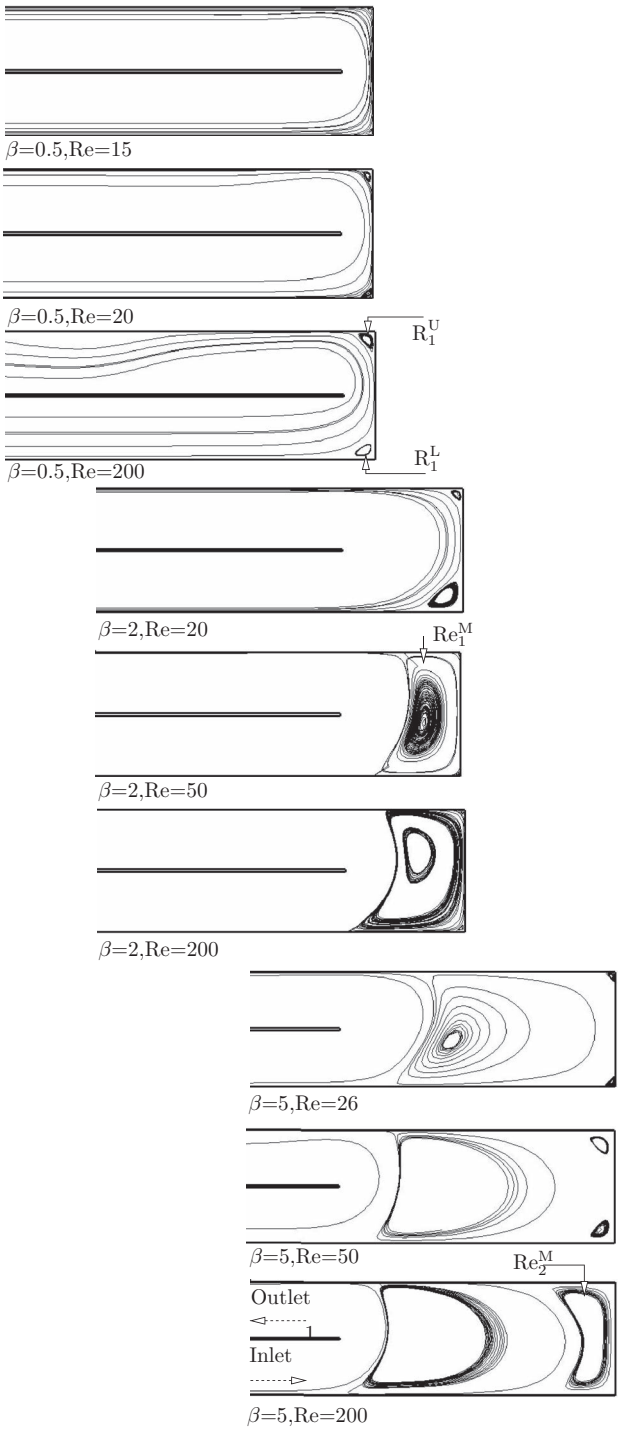

FIG. 21. Flow regimes of the turning part section of 180° sharp bend.

This causes the recirculation to occupy an increasingly large part of the turning part of the bend, thus restricting the passage for the main stream. When $Re \geq 250$, the curve becomes flat and β^* is insensitive to Re. A similar trend was observed on the recirculation lengths (see Sec. IV B 2). It reflects that in these regimes, the flow topology does not evolve significantly in the turning part when Re is further increased. Remarkably, all curves $\beta^*(Re)$ collapse into a single one $\beta^N(Re)$ shortly after the appearance of the first recirculation, which confirms that in this regime, the position of the

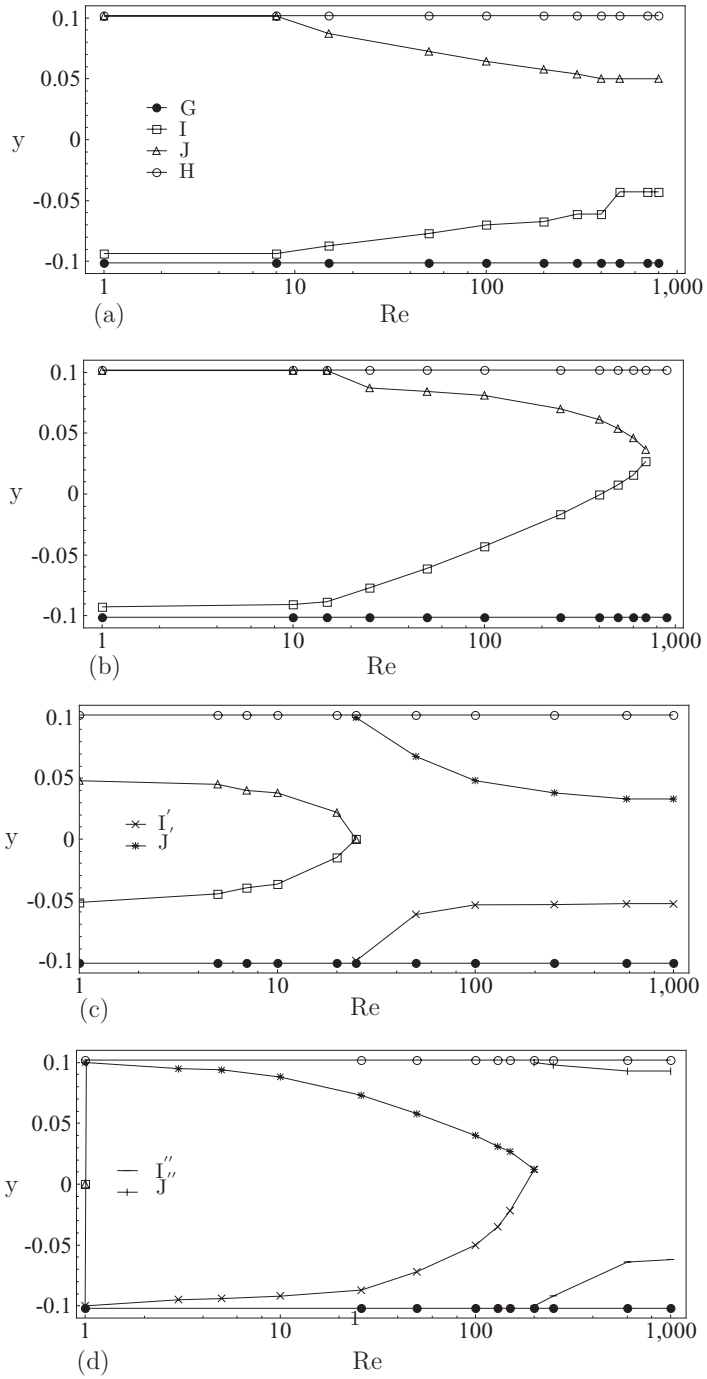

FIG. 22. Time average of separation and re-attachment points in the turning part area of the bend vs. Re. (a) $\beta = 0.5$, (b) $\beta = 1$, (c) $\beta = 3$, and (d) $\beta = 5$.

outer wall does not influence the flow topology in the main stream. At large values of Reynolds, β^N saturates around the value of 0.7, which therefore represents the "natural" extension required by the flow to turn from inlet to outlet directions.

A second noticeable feature of the curves $\beta^*(Re)$ is that around each point where a new merging occurs, all of them overshoot the universal curve $\beta^N(Re)$ before rejoining it. This means that in the overshoot region, the flow extends a little further than its "natural" width. Indeed, for a recirculation

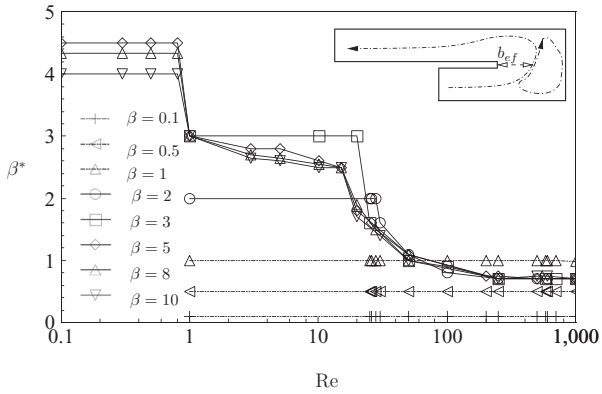

FIG. 23. β^* vs. Re for different β.

to exist in this regime, it has to be strongly elongated in the $\mathbf{e}_y$ direction, with extreme streamline curvatures. A dedicated stability analysis is needed to determine the actual conditions of appearance of such a flow but our results suggest that such a solution may not be stable. Interestingly, for values of β slightly greater than β^* (see curve for $\beta = 1$), the overshoot extends over the whole range of values of Re we explored. In terms of design, values of β that place the flow in the overshoot region are therefore optimal, since they make it possible to extend the main stream width beyond its "natural" width, thus reducing local head losses, without incurring any energy loss in driving extra recirculations in the turning part.

VI. FLOW IN A 3D 180° SHARP BEND

We shall now evaluate the relevance of the 2D dynamics analysed in Secs. II–V to the full 3D flow. To this end, we simulate the flow in the configuration sketched in Fig. 24. This geometry is identical to that considered for the 2D simulations (Fig. 2) in the (x, y) plane but the domain now extends by $2a$ in width (dimensionally, in the z direction). Periodic boundary conditions are applied at $z = -1$ and $z = 1$, while other boundary conditions remain those enforced previously (see Sec. II). The corresponding 3D mesh was obtained by extrusion along z of mesh M4, with 40 equidistantly spaced points along z (grid size 0.05), so that (y, z) sections of cells near the duct centreline are squares (see Fig. 25). To make sure the that these choices of resolution and domain width have a limited influence on the results, two extra simulations are carried out. For the first test case (TC1), we increase the mesh resolution in the spanwise resolution to 80 equidistantly spaced points, while keeping the same width of $2a$. For the second test case (TC2), we increase the spanwise length from $2a$ to $4a$ without increasing the resolution. Both simulations are performed at $\mathrm{Re} = 2000$ for $\beta = 1$. The relative discrepancies on the time averaged of C_d and C_l (on the inside boundary) between TC1, TC2, and the case with 40 points over a spanwise length of $2a$ (C0) are reported in Table II: they all remain around 1%. We also compared the Strouhal number S_t built on the main

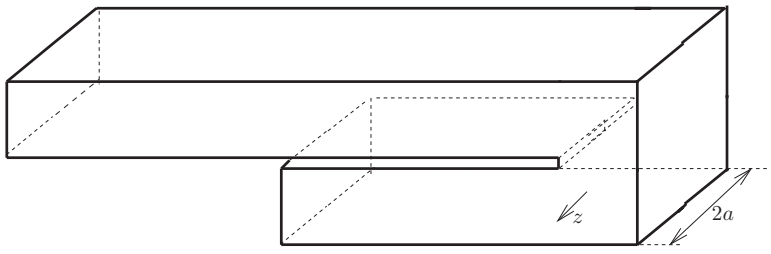

FIG. 24. Sketch of 3D geometry.

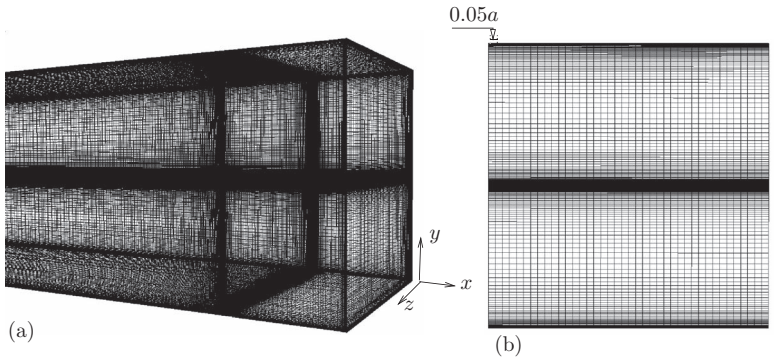

FIG. 25. Details of the meshes for 3D geometry: (a) domain near the turning part and (b) mesh view from the end wall.

shedding frequency (obtained as the dominant peak in the time-FFT of C_l). The relative discrepancy turns out to be very small as well (see Table II). This confirms that results obtained with (C0) are sufficiently precise for the purpose of this work. The high computational cost of unsteady 3D numerical simulations makes it impossible to reproduce the 2D simulations in 3D. Instead, we shall target a limited representative number of cases: a reduced incremental analysis was conducted for $\beta = 1$ (Re = 400, 1000, 1500, 2000) where the flow was initialised in the established state at the preceding Reynolds number. To probe regimes of high and low β, further simulations were performed at $\beta = 0.2$ (Re = 65, 520) and $\beta = 5$ (Re = 400, 500, 2000), where the flow was initialised in the state found in the 2D computations in order to avoid the computationally prohibitive computational cost incurred by the transient in these regimes.

Figs. 26 and 27(a) show the streamlines for cases above where the flow was steady. In all instances, the flow remained perfectly 2D, and the corresponding 2D flow was identical to that found in the 2D simulations for all three values of β, in both the turning and the outlet parts, and whether in regime II ($\beta = 0.2$, Re = 65 in Fig. 29(a)) or III ($\beta = 1$, Re = 400 in Fig. 26(a) and $\beta = 5$, Re = 400 in Fig. 27(a)). This was further confirmed after comparing the values of C_d and C_l with width units, L_1 and L_2 to those previously obtained (see Table III).

For $\beta = 1$, the flow was found unsteady at Re = 1000: as in 2D simulations, the shear layer between the two steady recirculations becomes unstable and sheds structures that extend across the whole width of the duct. This phenomenology is that of regime IV, with two noticeable differences: first, three-dimensionality is present under two forms: the shed structures show a long-wave oscillation along the z direction reminiscent of 3D A-modes,[37] which appear when Von Karman streets become 3D. These are complemented by elongated streamwise vorticity filaments woven around shed vortices, similar to B-modes.[38] Further downstream, 3D instabilities eventually disrupt the initially 2D vortex. This impedes the growth of shed vortices and limits their interaction with the walls. Since this effect was responsible for the shedding of the first recirculation in regime V, transition to this regime was found in none of the subsequent simulations at $Re = 1500$ nor $Re = 2000$ (see Figs. 26 and 27(b)). Nevertheless, 3D instabilities develop more intensively as Re increases and progressively take over the role of disrupting the train of shed vortices played by vortex-wall interactions in regime V found in 2D simulations. When Re reaches $Re = 2000$ any 2D section of the 3D flow in an (x, y) plane has become very similar to its 2D counterpart, and the

TABLE II. Comparison of C_d, C_l, and S_t for different resolutions and domain widths at Re = 2000 for $\beta = 1$. C_d and C_l are expressed per width of $2a$. The superscript *err* stands for relative discrepancies to the reference case (C0).

Case	Domain width along z	Points along z	C_d	C_d^{err} (%)	C_l	C_l^{err} (%)	S_t	S_t^{err} (%)
C0	$2a$	40	3.37×10^{-2}	...	3.915	...	5.05×10^{-2}	...
TC1	$2a$	80	3.325×10^{-2}	1.33	3.895	0.05	5.13×10^{-2}	1.58
TC2	$4a$	80	3.405×10^{-2}	1.03	3.92	0.13	4.97×10^{-2}	1.56

TABLE III. Comparison of L_1, L_2, C_d, C_l, and discrepancy between 2D and 3D simulations. Quantities from 3D simulations are expressed per unit length.

	L_1^{2D}	L_1^{3D}	L_1^{err} (%)	L_2^{2D}	L_2^{3D}	L_2^{err} (%)	C_d^{2D}	C_d^{3D}	C_d^{err} (%)	C_l^{2D}	C_l^{3D}	C_l^{err} (%)
$\beta = 0.2$												
$\mathrm{Re} = 65$	2.1	2.05	2.4	1.1	1.06	3.6	1.85×10^{-2}	1.94×10^{-2}	4.6	2.75	2.65	3.6
$\mathrm{Re} = 520$	1.12	1.09	2.6	...	...	...	8.4×10^{-3}	8.1×10^{-3}	3.5	1.83	1.76	3.8
$\beta = 1$												
$\mathrm{Re} = 400$	4.4	4.3	2.3	4.31	4.2	2.5	0.31×10^{-2}	0.3×10^{-2}	3.2	2.3×10^{-1}	2.3×10^{-1}	0.4
$\mathrm{Re} = 2000$	...	...	...	...	...	...	1.76×10^{-3}	1.69×10^{-3}	3.9	1.88×10^{-1}	1.96×10^{-1}	4.5
$\beta = 5$												
$\mathrm{Re} = 500$	4.4	4.28	2.7	4.71	4.61	2.1	3.02×10^{-3}	2.93×10^{-3}	2.7	2.5×10^{-1}	2.4×10^{-1}	2.7
$\mathrm{Re} = 2000$	...	...	...	...	...	...	1.72×10^{-3}	1.68×10^{-3}	2.3	1.85×10^{-1}	1.9×10^{-1}	2.7

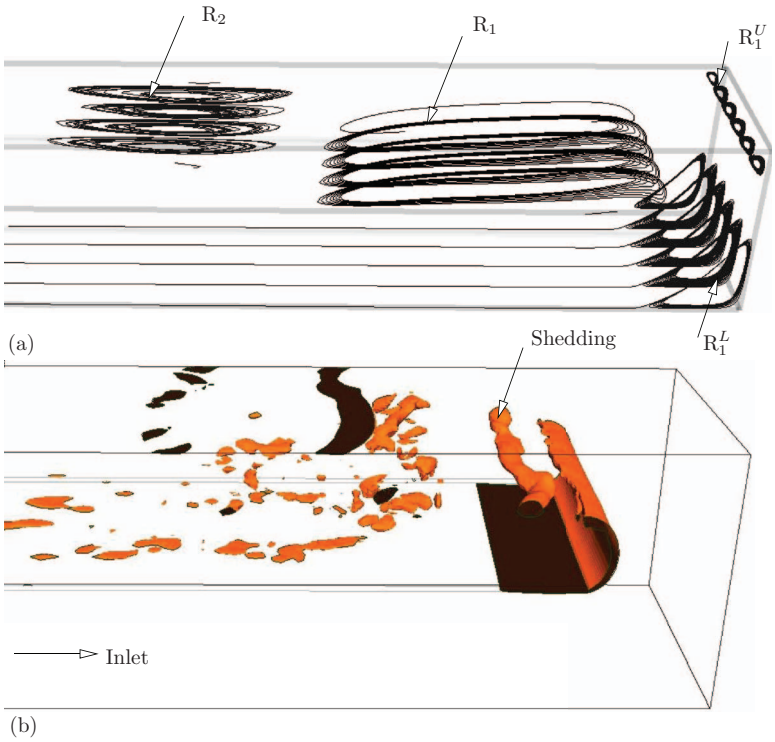

FIG. 26. Velocity streamlines (a) for Re = 400 and iso-surfaces of z-vorticity [$\omega_z = 0.025\omega_{zmax}$] and (b) for Re = 2000 at $\beta = 1$.

values of C_d, C_l, and L_1 from 2D and 3D simulations have become very close again. The Strouhal number found in 3D simulations, however, is lower than in the 2D ones: this is due to 3D instabilities impeding the shedding mechanism (in the same way as wall interaction did in Sec. IV C 2). This effect is the main consequence of the three-dimensionality, which can therefore be detected through its signature on S_t and its variations. These two-dimensional shedding structures are obtained in

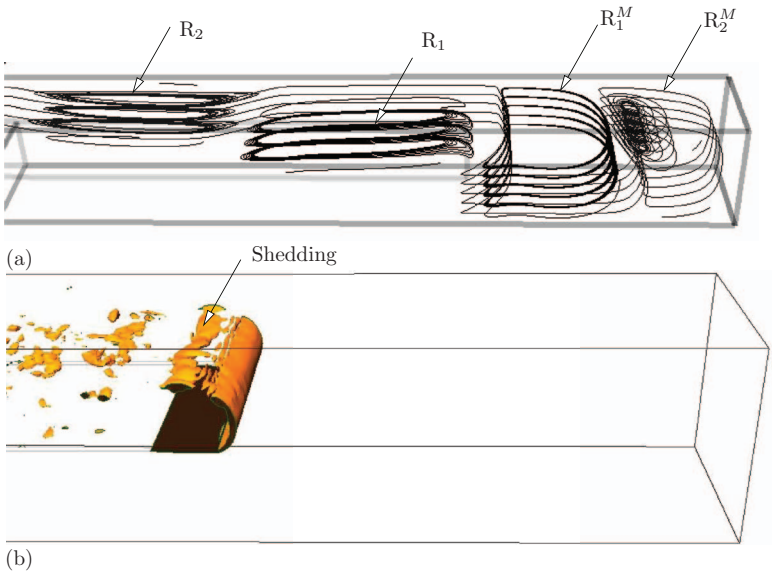

FIG. 27. Velocity streamlines (a) for Re = 500 and iso-surfaces of z-vorticity [$\omega_z = 0.027\omega_{zmax}$] and (b) for Re = 2000 at $\beta = 5$.

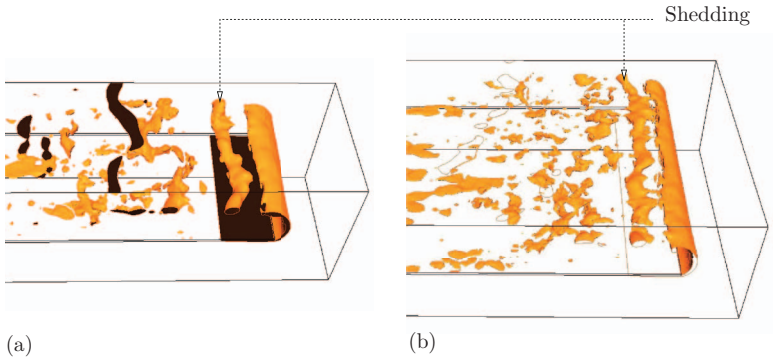

FIG. 28. Iso-surfaces of z-vorticity for Re = 2000 at $\beta = 1$: (a) TC1 [$\omega_z = 0.025\omega_{zmax}$] and (b) TC2 [$\omega_z = 0.023\omega_{zmax}$].

simulation C0 and also in TC2, where the spanwise length is $4a$ (see Fig. 28), which is an evidence of the robustness of this phenomenon.

Simulations of unsteady flows at $\beta = 0.2$ and $\beta = 5$ (see Figs. 29(b) and 27(b)) return a picture that is consistent with this scenario. At $\beta = 0.2$, however, regimes IV and V were practically indistinguishable in 2D simulations. 2D sections of 3D simulations accordingly coincide with 2D simulations even for mildly supercritical unsteady flows, and so do C_d, C_l, L_1, and S_t. In particular, the "wheel" structure of recirculation R_1 is present in both cases and identical in shape and dynamics in 2D and 3D simulations, despite the presence of smaller 3D structures (see Fig. 30). From a practical point of view, this implies that even when the flow is strongly 3D, 2D simulations are sufficient to recover global quantities and capture the overall dynamics of the flow, with the exception of the early stages of regime V, at moderate to high values of β. Finally, it should be noted that the flow in the turning part remained steady and identical to the flow found in the 2D simulation in all 3D simulations, whether the flow was steady or not in the outlet part.

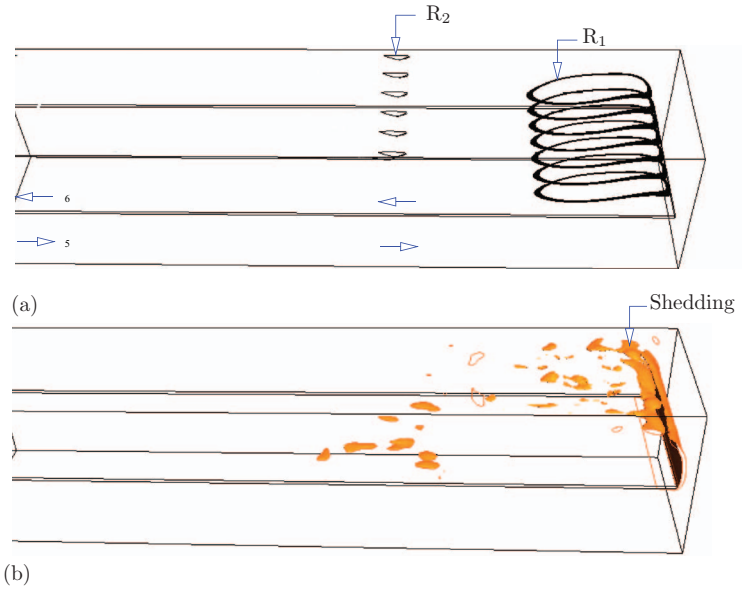

FIG. 29. Velocity streamlines (a) for Re = 65 and iso-surfaces of z-vorticity [$\omega_z = 0.027\omega_{zmax}$] and (b) for Re = 520 at $\beta = 0.2$.

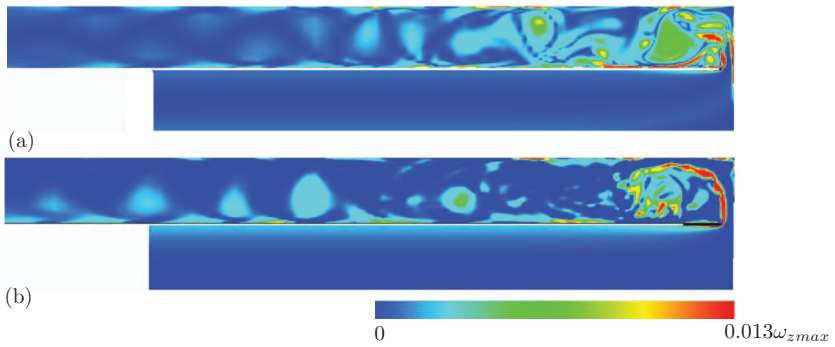

FIG. 30. Snapshot of vorticity contours taken from the 2D simulation (a) and 3D simulation (b) for Re = 520 at $\beta = 0.2$. Even though the flow is strongly 3D, the general structure of the flow is very similar in both simulations, with in particular, a large 2D recirculation R_1, acting as "wheel," which conveys smaller structures generated by the instability of the jet that wraps around it. Values of C_d, C_l, L_1, and St found in the 2D and 3D simulations are accordingly very close to each other.

VII. CONCLUSION

We have conducted a systematic numerical study of the influence of the geometry on the flow in a sharp 180° bend. Parametrizing the geometry with the sole opening ratio β made it possible to conduct a detailed parametric analysis of the 2D flow features, complemented by targeted 3D simulations. This combined approach unveiled a wealth of complex steady and unsteady 2D regimes with vastly different features, which we found to be either fully or at least partially relevant to 3D geometries. These can be broadly summarised as follows.

The flow results from the combined dynamics of two distinct regions of the bend: the outlet part on the one hand, and the turning part on the other hand. When increasing the opening ratio, and thereby the size of the turning part, the 2D flow evolves from a jet regime where the whole stream passes within a thin layer injected in the outlet, to a more classical turning channel flow. If the passage is opened wider than the inlet/outlet channel width, then as the Reynolds number is increased, the flow in the turning part is reorganized in a main stream with an effective opening ratio β^* that tends toward $\beta^* \simeq 0.7$, while the rest of the turning part is filled with alternately rotating cells. Only at low Reynolds numbers is it possible to take advantage of a turning part with $\beta > 1$ to spread the flow over a wider section. In this regard, the relation between β^* and Re, provides a guideline to optimise the design of systems involving 180° bends for a particular application.

The greatest complexity was found in the dynamics of the outlet branch. The succession of regimes encountered when increasing Re is reminiscent of that found in the wake of 2D cylinder in many respects. Nevertheless, the strong confinement imposed by the channel walls and the absence of symmetry with respect to the channel centreline incurred a number of highly specific features. First, the two steady recirculations, that appear along either walls of the outlet, do so successively, in the sense of increasing Reynolds numbers. Second, they destabilise in radically different ways in jet-like flows ($\beta \leq 0.2$) than they do in channel-like flows ($\beta \geq 0.3$). In both cases, unsteadiness appears when the shear layer that carries the main stream between the two recirculations undergoes a Kelvin Helmholtz instability, that leads the flow into a chaotic state. The channel-type flow then enters a regime of vortex shedding where the upstream-most recirculation is turned into a vortex formation akin to that found behind 2D obstacles. The shed vortices released downstream are of comparable size to the width of the channel, and incur strong vortex separation at both walls of the channel with transverse plumes extending across it. Such a regime can be expected to favour highly effective heat transfer between these walls, and is therefore relevant to the design of heat exchangers. In the jet regimes, by contrast, transition to turbulence occurs through the Kelvin-Helmholtz instabilities affecting both recirculations. These lead to intense small scale turbulence, even at moderately high Reynolds numbers (of the order of 10^3). Such regimes are of more interest in mixing applications than in heat transfer.

Selected 3D simulations in a wide bend suggest that steady regimes are identical in 2D and 3D but that three-dimensionality appeared at the onset unsteadiness. The main difference, for $\beta = 1$, was that 3D instabilities prevent the interactions between large vortices and the walls that lead to the brutal transition to regime V in 2D. Nevertheless, outside of the early stages of this regime, 2D simulations reproduce the overall dynamics of the flow correctly and recover global parameters (drag, lift, recirculation length) to a good precision. The main effect of three-dimensionality is to impede vortex shedding, which translates into a lower value of the Strouhal number in 3D than in 2D. In the turning part of the bend, the flow remained steady and 2D in all investigated cases. Therefore, on the top of their relevance to flows with a purely 2D dynamics such as MHD flows or thin bends, 2D simulations are therefore able to capture the main features of 3D flows too.

ACKNOWLEDGMENTS

This work was supported by a Coventry University China Collaborative Fellowship and the Chinese Scholar Council.

[1] B. F. Armaly, F. Durst, J. C. F. Pereira, and B. Schonung, "Experimental and theoretical investigation of backward-facing step flow," J. Fluid Mech. **127**, 473 (1983).
[2] J. Y. Hwang and K. S. Yang, "Numerical study of vortical structures around a wall-mounted cubic obstacle in channel flow," Phys. Fluids **16**, 2382 (2004).
[3] I. E. Barton, "Laminar flow over a backward-facing step with a stream of hot particles," Int. J. Heat Fluid Flow **18**, 400 (1997).
[4] M. A. Abdou, M. S. Tillack, and A. R. Raffray, "Thermal, fluid flow, and tritium release problems in fusion blankets," Fusion Technol. **18**, 165 (1990).
[5] T. S. Wang and K. Mingking, "Heat convection in a 180-deg turning duct with different turn configurations," J. Thermophys. Heat Transfer **8**, 595 (1994).
[6] M. Hirota, H. Fujita, A. Syuhada, S. Araki, T. Yoshida, and T. Tanaka, "Heat/mass transfer characteristics in two-pass smooth channels with a sharp 180-deg turn," Int. J. Heat Mass Transfer **42**, 3757 (1999).
[7] D. E. Metzger and M. K. Sahm, "Heat transfer around sharp 180-deg turns in smooth rectangular channels," J. Heat Transfer **108**, 500 (1986).
[8] T. Astarita and G. Cardone, "Thermofluidynamic analysis of the flow in a sharp 180-deg turn channel," Exp. Therm. Fluid Sci. **20**, 188 (2000).
[9] T. M. Liou, C. C. Chen, Y. Y. Tzeng, and T. W. Tsai, "Non-intrusive measurements of near-wall fluid flow and surface heat in a serpentine passage," Int. J. Heat Mass Transfer **43**, 3233 (2000).
[10] T. M. Liou, Y. Y. Tzeng, and C. C. Chen, "Fluid flow in a 180-deg sharp turning duct with different divider thicknesses," ASME J. Turbomach. **121**, 569 (1999).
[11] M. K. Chyu, "Regional heat transfer in two-pass and three-pass with 180-deg sharp turns," J. Heat Transfer **113**, 63 (1991).
[12] Y. M. Chung, P. G. Tucker, and D. G. Roychowdhury, "Unsteady laminar flow and convective heat transfer in a sharp 180° bend," Int. J. Heat Fluid Flow **24**, 67 (2003).
[13] M. M. Zdravkovich, *Flow Around Circular Cylinders. Vol. 1: Fundamentals* (Oxford University Press, Oxford, 1997).
[14] M. Sahin and R. G. Owens, "A numerical investigation of wall effects up to high blockage ratios on two-dimensional flow past a confined circular cylinder," Phys. Fluids **16**, 1305 (2004).
[15] N. Nait Bouda, R. Schistel, M. Amieth, C. Rey, and T. Benabid, "Experimental approach and numerical prediction of a turbulent wall jet over a backward facing step," Int. J. Heat Fluid Flow **29**, 927 (2008).
[16] F. Schafer, M. Breuer, and F. Durst, "The dynamics of the transitional flow over a backward-facing step," J. Fluid Mech. **623**, 85 (2009).
[17] H. K. Moffatt, "Viscous and resistive eddies near a sharp corner," J. Fluid Mech. **18**, 1 (1964).
[18] H. K. Moffatt, "Viscous eddies near a sharp corner," Arch. Mech. Stosow. **16**, 365 (1964).
[19] W. M. Collins and S. C. R. Dennis, "Viscous eddies near a 90° and a 45° corner in a flow through a curved tube of triangular cross-section," J. Fluid Mech. **76**, 417 (1976).
[20] S. Mochizuki, A. Murata, R. Shibata, and W. J. Yang, "Detailed measurements of local heat transfer coefficients in turbulent flow through smooth and rib-roughened serpentine passages with a 180-deg sharp bend," Int. J. Heat Mass Transfer **42**, 1925 (1999).
[21] A. Oron, S. H. Davis, and S. G. Bankoff, "Long-scale evolution of thin liquid films," Rev. Mod. Phys. **69**, 931 (1997).
[22] D. Bensimon, L. P. Kadanoff, S. Liang, B. I. Shraiman, and C. Tang, "Viscous flows in two dimensions," Rev. Mod. Phys. **58**, 977 (1986).
[23] V. Dousset and A. Pothérat, "Numerical simulation of a cylinder wake under a strong axial magnetic field," Phys. Fluids **20**, 017104 (2008).
[24] S. Molokov and L. Buhler, "Liquid metal flow in a U-bends in a strong uniform magnetic field," J. Fluid Mech. **267**, 325 (1994).
[25] A. Pothérat, "Quasi-two dimensional perturbations in duct flows with a transverse magnetic field," Phys. Fluids **19**(7), 074104 (2007).

[26] R. Klein, A. Pothérat, and A. Alferenok, "Experiment on an electrically driven, confined vortex pair," Phys. Rev. E **79**(1), 016304 (2009).
[27] L. Biferale, S. Musacchio, and F. Toschi, "Inverse energy cascade in three-dimensional isotropic turbulence," Phys. Rev. Lett. **108**, 164501 (2012).
[28] T. E. Tezduyar and R. Shih, "Numerical experiments on downstream boundary of flow past cylinder," J. Eng. Mech. **117**, 854 (1991).
[29] M. Braza, P. Chassaing, and H. H. Minh, "Numerical study and physical analysis of the pressure and velocity fields in the near wake of a circular cylinder," J. Fluid Mech. **165**, 79 (1986).
[30] R. Issa, "Solution of the implicitly discretized fluid flow equations by operator-splitting," J. Comput. Phys. **62**, 40 (1986).
[31] V. Dousset and A. Pothérat, "Formation mechanism of hairpin vortices in the wake of a truncated square cylinder in a duct," J. Fluid Mech. **653**, 519 (2010).
[32] P. G. Drazin and W. H. Reid, *Hydrodynamic Stability* (Cambridge University Press, Cambridge, 1981).
[33] M. D. Ripley and L. L. Pauley, "The unsteady structure of two-dimensional steady laminar separation," Phys. Fluids **5**, 3099 (1993).
[34] L. L. Pauley, P. Moin, and W. C. Reynolds, "The structure of two-dimensional separation," J. Fluid Mech. **220**, 397 (1990).
[35] R. L. Davis and I. E. Carter, "Analysis of arifoil transitional separation bubbles," NASA CR 3791, 1984.
[36] M. Frank, L. Barleon, and U. Müller, "Visual analysis of two-dimensional magnetohydrodynamics," Phys. Fluids **13**, 2287 (2001).
[37] M. Brede, H. Eckelmann, and D. Rockwell, "On secondary vortices in the cylinder between parallel planes," Phys. Fluids **8**, 2117 (1996).
[38] R. D. Henderson, "Nonlinear dynamics and pattern formation in turbulent wake transition," J. Fluid Mech. **352**, 65 (1997).